Petroleum Science 23 (2026) 17–32

Contents lists available at ScienceDirect

Petroleum Science

journal homepage: www.keaipublishing.com/en/journals/petroleum-science

Original Paper

Insight into porosity of shale oil reservoirs: Comparison of helium, low-temperature nitrogen adsorption–desorption, and nuclear magnetic resonance methods

Jun-Jie Wang [a,b], Peng-Fei Zhang [a,b,*], Shuang-Fang Lu [a,b], Wei-Zheng Gao [a,b], Neng-Wu Zhou [a,b], Wen-Biao Li [a,b], Guo-Hui Chen [a,b]

[a] Sanya Offshore Oil & Gas Research Institute of Northeast Petroleum University, Sanya, 572025, Hainan, China
[b] State Key Laboratory of Continental Shale Oil, Northeast Petroleum University, Daqing, 163318, Heilongjiang, China

ARTICLE INFO

Article history:
Received 16 April 2025
Received in revised form
30 June 2025
Accepted 2 September 2025
Available online 6 September 2025

Edited by Jie Hao and Xi Zhang

Keywords:
Shale oil
Helium porosity
Low-temperature nitrogen adsorption–desorption
Nuclear magnetic resonance

ABSTRACT

Porosity is a fundamental parameter in characterizing the pore structure of shale oil reservoirs, as it directly affects the accuracy of shale oil reserve estimations. Despite the availability of various measurement techniques, accurately quantifying porosity in such reservoirs remains a significant challenge. In an effort to identify the most effective porosity testing method, this study collected samples from four shale oil reservoir intervals across five sags in three different basins. Five porosity testing methods were employed to detect shale porosity, including helium porosity, low-temperature nitrogen adsorption–desorption (LTNA/D), oil-saturated wetting, and nuclear magnetic resonance (NMR) T_2 and T_1–T_2. NMR T_2 porosity acted as a touchstone against which the other methods were compared. The pros and cons of each evaluation technique were explored to select the optimal analysis method for shale oil reservoirs. Results indicate that LTNA/D porosity, derived from powdered samples, commonly fails to reflect shale porosity effectively. Helium porosity, widely used for detecting nanoscale pores, is constrained by extended equilibration times and the retention of residual pore fluids after oil washing and drying, leading to systematic underestimation. In contrast, oil-saturation wetting and NMR T_2 exhibit strong agreement, both reflecting pore fluid content. However, residual fluid distribution can also impact the accuracy of NMR T_2 measurements. NMR T_1–T_2 is an innovative technique for quantitatively evaluating shale oil reservoirs. NMR T_1–T_2 spectrum at the water and oil restoration state can provide accurate shale porosity. NMR T_1–T_2 porosity estimates generally align with those obtained from T_2 porosity. When residual pore fluids are not entirely removable, the NMR T_1–T_2 method offers a more realistic porosity assessment. The NMR technique is recommended for evaluating the porosity of shale oil reservoirs, and the combination of T_2 and T_1–T_2 can accurately determine the effective and total porosity. This research serves as a valuable reference for accurately determining porosity in shale oil reservoirs.

1. Introduction

Shale oil and gas, as a pivotal alternative to conventional hydrocarbon resources, have undergone a series of successful explorations, significantly propelling the “shale revolution” (Li W.B. et al., 2024; Suo et al., 2024; Zhao W.Z. et al., 2024). The substantial resource potential of shale oil has attracted growing attention. Reserve assessment is crucial for shale oil exploration, typically conducted via mass oil content and volumetric methods (Jarvie, 2012; Wang et al., 2022a). The mass oil content method relies on the oil content (such as S_1 or chloroform asphalt “A”) and the mass of the shale oil reservoir series (Jarvie, 2012). In contrast, the volumetric method is considered more accurate and is recommended for evaluating shale oil reserves (Wang et al., 2022b). Key steps for the volumetric method involve obtaining porosity

* Corresponding author.
E-mail address: zhangpengfei@nepu.edu.cn (P.-F. Zhang).
Peer review under the responsibility of China University of Petroleum (Beijing).

https://doi.org/10.1016/j.petsci.2025.09.004

and oil saturation, with accurate shale porosity testing being crucial.

Porosity is a critical parameter for characterizing the pore structure of shale reservoirs, as it fundamentally reflects the pore volume. Various techniques have been developed to detect shale porosity, including helium porosity, gas adsorption, mercury intrusion capillary pressure (MICP), small-angle and ultra-small-angle neutron scattering (SANS/USANS), saturated wetting, and one-dimensional nuclear magnetic resonance (NMR) T_2 methods (Clarkson et al., 2012; Li et al., 2019; Zhang et al., 2018, 2022; Fan et al., 2023; Suo et al., 2025). Among these, helium porosity is considered one of the most accurate and commonly used methods (Zhang et al., 2022). Helium, as a non-adsorbing gas with an extremely small molecular diameter, can easily penetrate the nanopore networks of shale, enabling effective pore volume detection. Gas adsorption, primarily low-temperature nitrogen adsorption-desorption (LTNA/D) for shale oil reservoirs, analyzes pores less than 200 nm and determines the total pore volume (Wang et al., 2023, 2025). Correspondingly, LTNA/D porosity is inferred from total pore volume and typically excludes larger pores (Zargari et al., 2015). MICP specializes in measuring the volume of connected pores (Hu et al., 2017), while SANS/USANS can determine both total and connected pore volumes (Clarkson et al., 2012). The saturated wetting method is the simplest approach, where porosity is estimated by comparing sample masses in the saturated and dry states (Yao et al., 2010; Zhang et al., 2022). However, its accuracy is significantly influenced by the choice of probe fluid (Chen et al., 2020). Hydration-induced secondary microfractures may form when shale is saturated with water or alcohol (Zhang et al., 2020). Therefore, saturation with oils such as kerosene or *n*-dodecane is generally recommended (Chen et al., 2020).

As a non-destructive and efficient detection technique, NMR has been widely utilized for characterizing the pore structure of shale reservoirs (Li et al., 2019; Elsayed et al., 2022; Zhang Y.Q. et al., 2025). Based on the NMR T_2 spectrum, a precise shale porosity testing technology has been provided (Zhang et al., 2022; Li et al., 2023). Correspondingly, NMR T_2 porosity exhibits excellent consistency with oil-saturated wetting porosity (Zhang et al., 2022). However, the aforementioned methods are all constrained by residual fluids in shale pores, except for SANS/USANS. A lower porosity will be obtained if residual pore fluids cannot be removed entirely. High-resolution scanning electron microscopy (SEM) images can directly disclose shale pore distributions. Surface porosity derived from SEM imaging has been employed to describe the shale pore contents. Unfortunately, surface porosity has significant uncertainty due to the influence of resolution and shale heterogeneity (Tian et al., 2021, 2022).

The microscopic occurrence of fluids in shale oil reservoirs has recently received increasing attention. The two-dimensional NMR T_1–T_2 technique is an alternative and innovative method for exploring the intricate distributions of pore fluids in shale oil reservoirs, enabling quantitative assessment of the states of pore oil and water (Fleury and Romero-Sarmiento, 2016; Habina et al., 2017; Li et al., 2022; Bai et al., 2025). Accordingly, the volumes of pore water and oil in shale pore networks can be quantified, providing a valuable tool for porosity evaluation in shale oil reservoirs (Li J.L. et al., 2024). After water and oil restoration, shale porosity can be calculated from the T_1–T_2 spectrum (Xiang et al., 2024). A key advantage of the NMR T_1–T_2 method is its ability to evaluate porosity without removing residual fluids from the pores, making it suitable for determining the original porosity of shale reservoirs. Nevertheless, NMR measurements are significantly influenced by testing parameters.

Nevertheless, few studies have conducted a comparative analysis of different porosity measurement techniques. Identifying the optimal porosity testing method for the diverse range of shale oil reservoirs remains a persistent challenge. To address this, a comprehensive study was carried out, involving the collection of samples with varying lithologies from four shale oil reservoir intervals across five sags in three different basins. The aim was to determine the most effective method for porosity evaluation. Five porosity analysis techniques were employed in this study, including helium porosity, LTNA/D, oil-saturated wetting, NMR T_2, and NMR T_1–T_2, to assess the porosity of shale oil reservoirs. NMR T_2 porosity was used as a reference for comparison with the other four methods. The applicability and limitations of each porosity measurement technique were discussed. This study contributes to the existing body of knowledge on shale oil reservoirs by highlighting the importance of selecting appropriate porosity measurement methods for different reservoir types.

2. Samples and methodology

2.1. Samples

In this study, a series of shale samples were collected from four formations across three basins. Specifically, 23 shale samples were selected from the Fourth Member of Funing Formation in the Gaoyou Sag, Subei Basin, denoted as GY-FN shales. The Subei Basin, located in eastern China, is part of the onshore region of the Subei-South Yellow Sea Basin (Zhang et al., 2024a). A total of 39 shales were gathered from the First Member of the Tengger Formation in the A'nan Sag, Erlian Basin, labeled as AN-TGE shales. And 45 shales were derived from the Fourth Member of the Aershan Formation in the Erennaoer Sag, Erlian Basin, categorized under NE-AES shales. In parallel, 29 and 33 shale samples were collected from the First Member of the Tengger Formation and the Fourth Member of the Aershan Formation, respectively, in the Wuliyasitai Sag, Erlian Basin, identified as WY-TGE and WY-AES shales. The Erlian Basin is located in Inner Mongolia, northeastern China (Zhang P.F. et al., 2025). Moreover, 12 shale samples were acquired from the Qingshankou Formation in the Gulong Sag, Songliao Basin, and are referred to as GL-QSK shales. The Songliao Basin is the largest lacustrine sedimentary basin in northeastern China (Bechtel et al., 2012). The selection of shales from diverse sedimentary environments is essential for investigating the variations in mineral compositions and organic matter contents, both of which significantly influence shale reservoir properties.

2.2. Experiments

All shale samples were initially cut into core plungers using wire cutting under anhydrous conditions. Each plunger was then further sectioned into two core plungers, approximately 35 mm in length, along with associated cuttings. One core plunger was used for helium porosity measurements, the other for NMR analysis, while SEM was performed on the cuttings. The surrounding material near the cutting sites was ground into powder for LTNA/D, X-ray diffraction (XRD), TOC, and Rock-Eval pyrolysis analyses. In addition, oil-saturated wetting porosity can be obtained based on the NMR experiments by comparing the qualities at different states. As a result, the impact of heterogeneity can be eliminated as much as possible. The experimental process is displayed in Fig. 1, and specific experiments are as follows.

Prior to the tests, the core plungers underwent a rigorous cleaning process for 14 days at a temperature of 85 °C and a pressure of 0.25 MPa, using the mixed solution of dichloromethane and acetone (3:1 in volume). Subsequently, the cores were dried in a vacuum oven at 110 °C for 24 h, then cooled to room temperature in a desiccator. Helium porosity was measured using a PoroPDP-

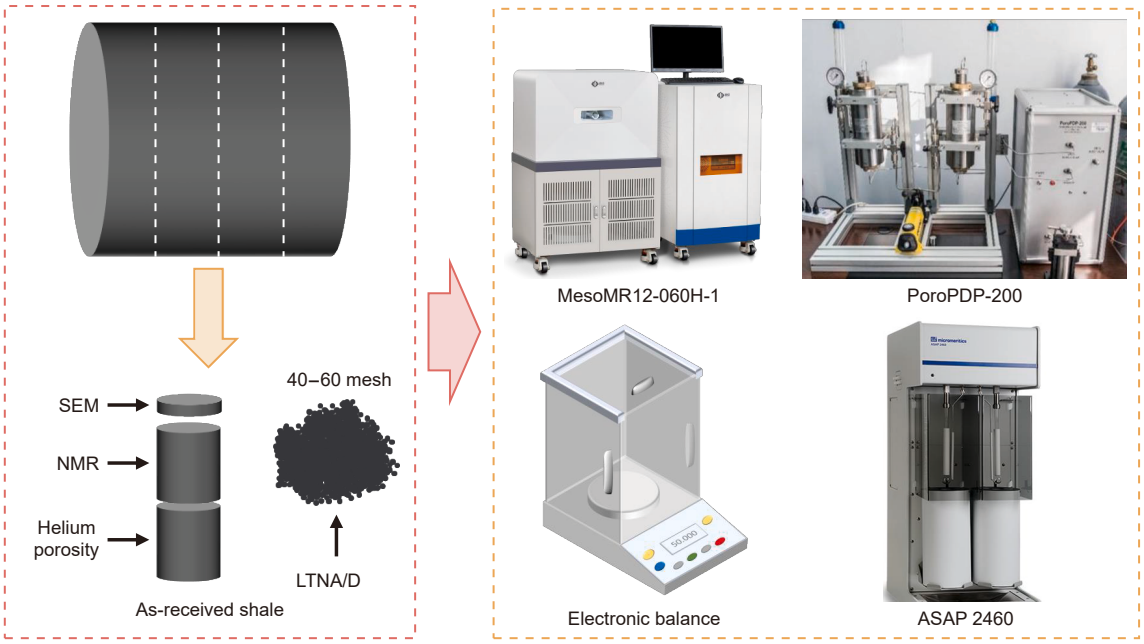

Fig. 1. Workflow of experimental processes.

200 porosity analyzer, which can determine the porosity ranging from 0.01% to 40.00%. Boyle's law can be used to obtain the pore volume, and the helium porosity is the ratio of pore volume to core volume. The diameters and lengths were first measured by a vernier caliper (0.01 cm). In this study, a test pressure of 200 psi and an equilibrium time of approximately 10 min were adopted. Helium porosity was directly obtained from the instrument. The helium porosity experiments referred to the National Standard of China (GB/T 34533–2017 Measurement of helium and pulse decay permeability of shale) (Xue et al., 2017).

The LTNA/D experiments were conducted on a Micromeritics ASAP 2460 surface area and porosity analyzer according to the oil and gas industry standard of China (SY/T 6154–1995 Measurement of specific surface area and pore size distribution of rocks: static nitrogen adsorption capacity method) (Wu et al., 1995). The Micromeritics ASAP 2460 has the micropore model with a 1 mmHg transducer, and nitrogen, argon, carbon dioxide, and other fixed gases can be used. The shale samples were crushed into powders with a particle size of 40–60 mesh and subjected to oil washing using the same procedure as described previously. The powdered samples were then dried under vacuum at 110 °C for 24 h. Nitrogen adsorption and desorption isotherms were obtained at 77 K, with relative pressures (P/P_0) ranging from 0.01 to 0.993, after the sample mass was accurately weighed with a precision of 0.0001 g. The total pore volume was determined based on the single-point pore volume.

NMR measurements were performed on five states, including as-received, water restoration, water and oil restoration, oil-washed and dry, and oil-saturated. These states have been described in detail in previous studies (Zhang et al., 2024a, 2024b). The as-received state refers to untreated samples, reflecting the distribution characteristics of residual pore fluids. Pore water was restored by exposing samples to high relative humidity (RH ≈ 0.98) until sample mass stabilized, allowing calibration of pore water NMR amplitude against the as-received state. Then, shale samples were saturated with light oil (*n*-dodecane) at 10 MPa for 24 h to achieve the water and oil restoration state, and NMR T_1–T_2 porosity can be determined. The samples were then washed and dried by the same procedure to provide reference states. Finally, dry shales were vacuumed for 24 h and saturated with *n*-dodecane at 10 MPa for 24 h to obtain the oil-saturated state. Based on this state, the amplitude of pore oil was calibrated, enabling the calculation of NMR T_2 porosity. T_2, T_1–T_2 spectra, and mass at five states were detected. Meanwhile, the oil-saturated wetting porosity can be determined by comparing the mass of shale in oil-saturated and dry states.

This study conducted the NMR experiments on a MesoMR12-060H-I NMR spectrometer (Niumag, China) with a resonance frequency of 12 MHz at a magnetic field of 0.3 ± 0.05 T. The T_2 and T_1–T_2 spectra were detected by the CPMG (Carr-Purcell-Meiboom-Gill) and SR (Saturation-recovery)-CPMG sequences, respectively. The test parameters were set as follows: TE (echo time) = 0.07 ms, TW (waiting time) = 3000 ms, NS (number of scans) = 32, NECH (echo number) = 4096, and NTI (number of inverse time) = 31 (Zhang et al., 2024a, 2024b).

2.3. Porosity evaluation methods

The LTNA/D porosity was determined according to the total pore volume and can be calculated as follows (Eq. (1)).

$$\varphi_N = V_N \cdot \rho_r \times 100\% \quad (1)$$

where φ_N refers to the LTNA/D porosity, %; V_N denotes the total pore volume obtained from LTNA/D, cm^3/g; ρ_r represents the rock density, g/cm^3.

According to the calibration equation, the amplitude of the NMR T_2 spectrum at the oil-saturated state after subtracting the dry state can be transformed to pore volume, and the NMR T_2 porosity (φ_{N1}) can be calculated by Eq. (2).

$$\varphi_{N1} = \frac{V_{o1}}{V_r} \times 100\% = \frac{A_{o1} \cdot k_o / \rho_o}{V_r} \times 100\% \quad (2)$$

where V_{o1} is the pore volume, cm^3; V_r represents the core volume, cm^3, which can be calculated by the diameter and length; A_{o1} refers to the amplitude of NMR T_2 spectrum at oil-saturated state after subtracting the amplitude at dry state, non-dimensional; k_o

denotes the calibration coefficient of pore oil, non-dimensional; ρ_o represents the oil density, g/cm^3.

Theoretically, the water and oil restoration state means that oil and water are completely saturated in the shale pore networks. Thus, the NMR T_1–T_2 spectrum has the ability to calculate porosity. The NMR T_1–T_2 porosity (φ_{N2}) is the sum of oil and water porosity, as described as follows.

$$\varphi_{N2} = \varphi_o + \varphi_w \tag{3}$$

$$\varphi_o = \frac{V_{o2}}{V_r} \times 100\% = \frac{A_{o2} \cdot k_o / \rho_o}{V_r} \times 100\% \tag{4}$$

$$\varphi_w = \frac{V_w}{V_r} \times 100\% = \frac{A_w \cdot k_w / \rho_w}{V_r} \times 100\% \tag{5}$$

where φ_o and φ_w are the oil and water porosity, respectively, %; V_{o2} and V_w refer to pore volumes saturated by oil and water, respectively, cm^3; A_{o2} and A_w are the amplitudes of pore oil and water in the NMR T_1–T_2 spectrum, respectively, non-dimensional; k_w denotes the calibration coefficient of pore water, non-dimensional; ρ_w represents the water density, g/cm^3.

Oil-saturated wetting porosity (φ_{ow}) can be easily calculated by comparing the qualities at dry and oil-saturated states (Eq. (6)).

$$\varphi_{ow} = \frac{V_{o1}}{V_r} \times 100\% = \frac{(m_o - m_d)/\rho_o}{V_r} \times 100\% \tag{6}$$

where m_o and m_d refer to the sample qualities at oil-saturated and dry states, respectively, g.

3. Results

3.1. Organic geochemical, mineral compositions, and pore types of shale samples

The TOC contents of the selected shales from various sags and formations are depicted in Fig. 2(a). All samples exhibit relatively high TOC values, with average contents exceeding 1%. The WY-TGE shales are distinguished by the highest TOC values, ranging from 0.44% to 5.05%, with a mean of 2.34%, followed by the GL-QSK shales, with the TOC content between 1.36% and 3.27% (mean 2.12%). WY-AES shales are the next, characterized by a mean of 1.50% (0.13%–4.12%), trailed by AN-TGE (mean 1.43%), GY-FN (mean 1.34%), and NE-AES (mean 1.21%) shales as follows. The GL-QSK shales have the largest S_1 values, with an average of 2.26 mg/g (1.32–4.82 mg/g), followed by WY-TGE (average 1.50 mg/g), AN-TGE (average 1.29 mg/g), WY-AES (average 1.17 mg/g), and GY-FN (0.88 mg/g) shales, as demonstrated in Fig. 2(b). Unfortunately, the NE-AES shales display the lowest S_1 values, with a mean of 0.83 mg/g. The relationships between S_2 and TOC, known as the hydrogen index (HI), indicate the organic matter types (Fig. 2(c)). The organic matter in the collected shales is predominantly categorized as Types II_1 and II_2. Notably, the AN-TGE shales exhibit a higher HI, consistent with Types I and II_1. In contrast, the WY-AES shales are mainly classified as Types II_2 and III, exhibiting the lowest HI values.

The mineral compositions of the studied shales in different sags vary significantly, as exhibited in Fig. 3. Shales from the A'nan and Erennaoer Sags are notable for their minimal clay mineral content, followed by those from the Gaoyou and Gulong Sags. In contrast, the clay mineral content in shales extracted from the Wuliyasitai Sag is considerably higher, particularly in the WY-AES shales, which exhibit a mean of 56.18%, ranging from 24.0% to 72.0% (Fig. 3(d)–(e)). The GL-QSK shales contain the highest quartz content, ranging from 31.8% to 37.8%, with a mean of 35.4%,

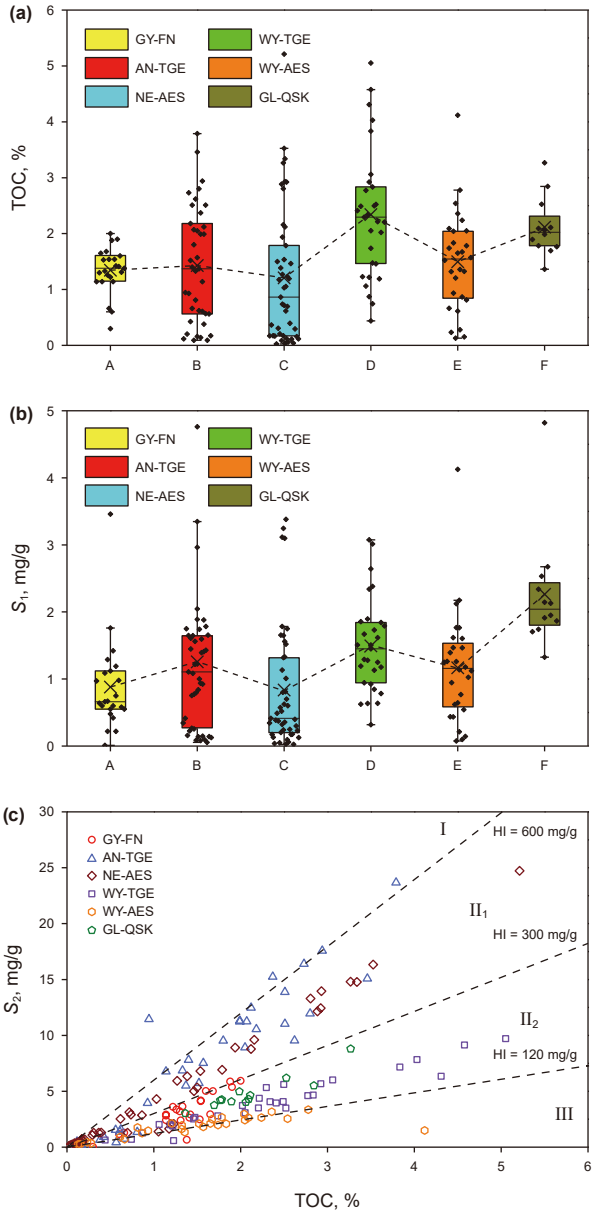

Fig. 2. TOC **(a)**, S_1 **(b)**, and organic matter types **(c)** of the selected shales.

whereas the NE-AES shales have the lowest quartz content, averaging 20.4% (range 5.0%–33.0%) (Fig. 3(c)–(f)). Additionally, the NE-AES shales show the highest feldspar content, varying between 12.0% and 45.0%, with a mean of 23.9% (Fig. 3(c)). Inversely, feldspar content is lowest in shales from the Wuliyasitai Sags (Fig. 3(d)–(e)). Elevated levels of calcite and dolomite mark shales in the Gaoyou, A'nan, and Erennaoer Sags, whereas shales in the Wuliyasitai and Gulong Sags are the opposite. Moreover, a substantial presence of siderite can be identified in WY-AES shales. The high concentrations of siderite and clay minerals in the WY-AES shales suggest deposition in a deep-water sedimentary environment (Ma et al., 2023; Wu et al., 2023).

Consequently, various lithologies can be identified in the selected shales according to the relative proportions of clay, felsic (quartz, feldspar, and orthoclase), and calcareous (calcite, dolomite, and siderite), as shown in Fig. 4. The GL-QSK shales are predominantly classified as carbonate-bearing argillaceous felsic-rich shales, while the samples from the Wuliyasitai Sag are

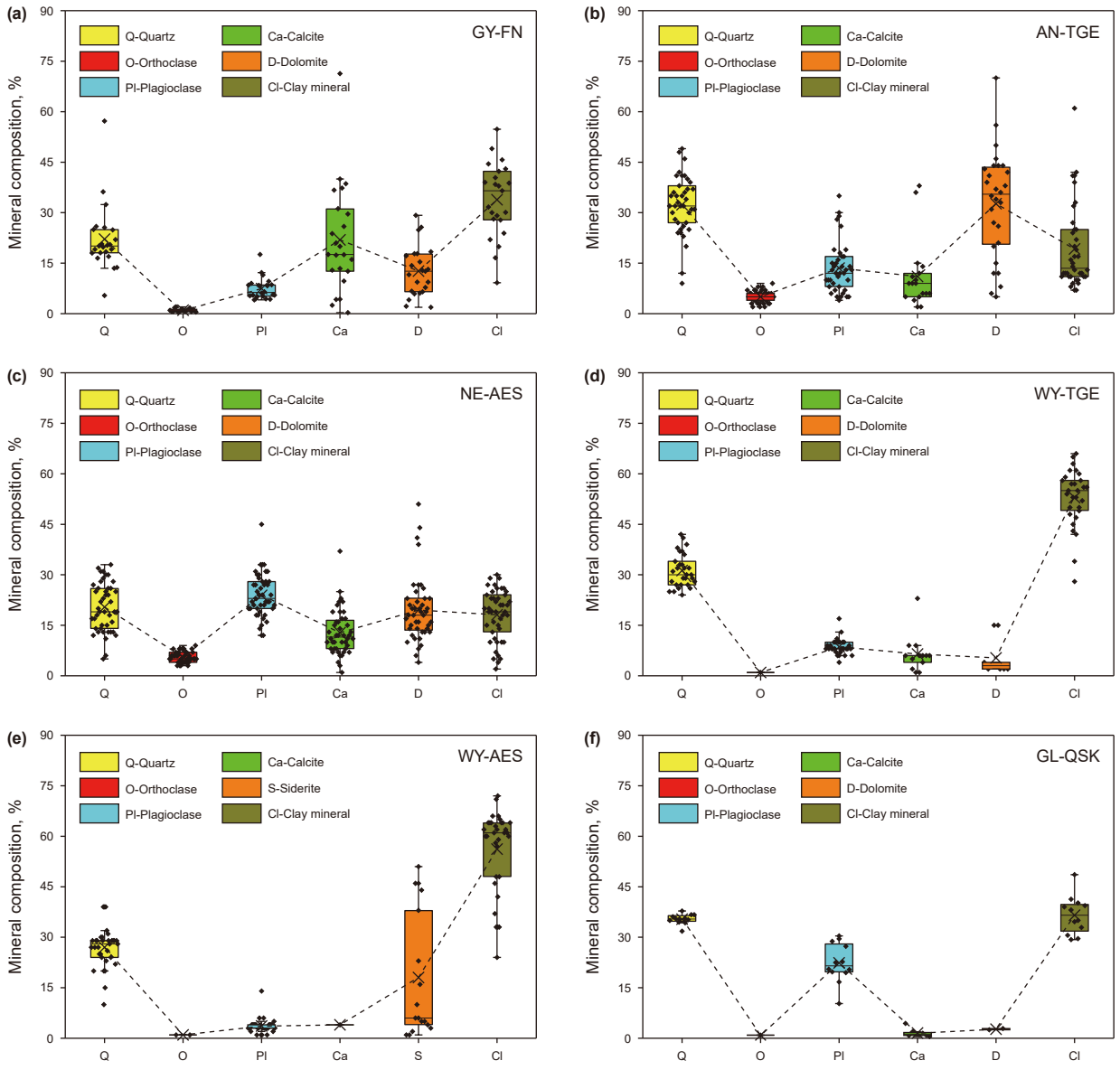

Fig. 3. Mineral compositions of the shale samples in different layers.

primarily identified as carbonate–bearing felsic argillaceous–rich shales. The GY-FN samples are generally typified by mixed shales, with argillaceous-calcareous mixed shales being the predominant type, closely followed by felsic-argillaceous mixed shales. The lithologies of AN-TGE shales exhibit frequent variation, with felsic-calcareous mixed being the most prevalent, followed by clay-bearing calcareous felsic-rich shales; a similar pattern is observed for the NE-AES shales.

Previous research has demonstrated that lithology is a key indicator of the paleosedimentary environment (Liu et al., 2023; Fan et al., 2024). Shales rich in calcite and dolomite, particularly dolomite, typically reflect arid to semi-arid, semi-saline to alkaline sedimentary settings. Conversely, the high clay mineral content in shale indicates warm-humid, brackish to freshwater, and deep-water conditions. Felsic shales are generally associated with warm-humid to semi-humid climates, brackish to freshwater, and shallow water environments. Consequently, the AN-TGE shales mainly correspond to a semi-arid to arid, semi-saline sedimentary environment, as do the NE-AES shales (Ding et al., 2015, 2016).

The paleo-sedimentary environment of the GY-FN shales is likely characterized by lower salinity levels (Fu et al., 2023), with relatively higher calcite and lower dolomite compared to the AN-TGE and NE-AES shales (Fig. 3). In contrast, the development of carbonate-bearing felsic argillaceous-rich shales in Wuliyasitai Sag implies a warm-humid, brackish to freshwater, and deep-water environment (Wu et al., 2023). Previous studies have indicated that the Qingshankou Formation shales were deposited in a warm-humid climate with brackish to freshwater conditions, akin to the Wuliyashitai Sag (Bechtel et al., 2012; Xu et al., 2019).

Various pores were observed in the selected shales, as exhibited in Fig. 5. Numerous interparticle pores between or along the edges of carbonate minerals can be identified in argillaceous-calcareous mixed shales. In contrast, felsic-argillaceous mixed shales, particularly from the Gaoyou Sag, are characterized by limited intraparticle pores within clay mineral aggregates and interparticle pores along the edges of felsic minerals (Fig. 5(a)–(b)). The high contents of felsic and calcareous minerals in AN-TGE shales result in the development of interparticle pores

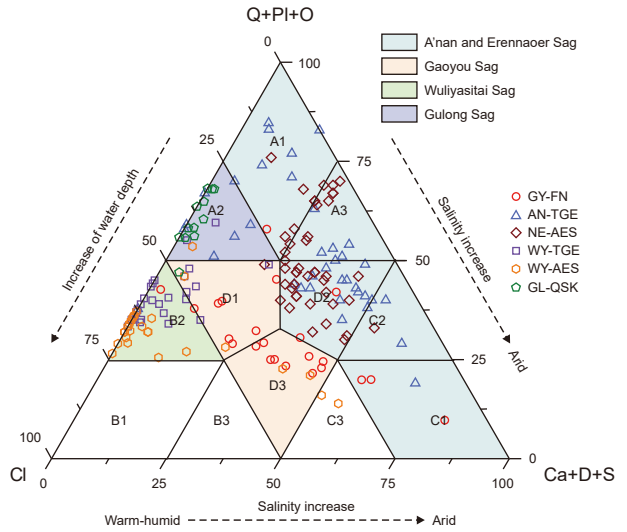

Fig. 4. Shale lithologies in different sags. Q, Pl, O, Cl, Ca, D, and S denote the quartz, plagioclase, orthoclase, clay mineral, calcite, dolomite, and siderite, respectively. A1, A2, and A3 are the felsic-rich, carbonate–bearing argillaceous felsic-rich, and clay-bearing calcareous felsic-rich shales; B1, B2, and B3 represent the argillaceous-rich, carbonate-bearing felsic argillaceous-rich, and felsic-bearing calcareous argillaceous-rich shales; C1, C2, and C3 refer to calcareous-rich, clay-bearing felsic calcareous-rich, and felsic-bearing argillaceous calcareous-rich shales; D1, D2, and D3 are felsic-argillaceous mixed, felsic-calcareous mixed, and argillaceous-calcareous mixed shales.

(Fig. 5(c)–(f)). As a result, interparticle pores between or at the edges of granules are most likely to appear in the felsic-calcareous mixed, carbonate-bearing argillaceous felsic-rich, felsic-rich, and clay-bearing calcareous felsic-rich shales. Moreover, a small number of dissolution pores occur in the felsic-rich and clay-bearing calcareous felsic-rich shales. A similar phenomenon is also present in the NE-AES shales, with the development of interparticle pores at the edges of granules, as displayed in Fig. 5(g) and (h). High contents of clay minerals in the WY-TGE, WY-AES, and GL-QSK shales are correlated with the widespread occurrence of intraparticle pores associated with these clay minerals (Fig. 5). Overall, the studied shales exhibit strong representativeness of lacustrine shale oil reservoirs, encompassing a wide range of mineral compositions and pore structures reflective of diverse sedimentary environments.

3.2. Helium and LTNA/D porosity

Fig. 6 displays the helium and LTNA/D porosity distributions of the selected shales. Helium porosity exhibits a trend broadly consistent with that of LTNA/D porosity. Specifically, the GL-QSK shales display the highest helium porosity, averaging 9.05% and ranging from 7.68% to 12.48%, which is attributed to the well–developed intraparticle pores within clay mineral aggregates (Fig. 5(k)–(l)). This is followed by AN-TGE (mean 5.44%), WY-AES (mean 4.33%), GY-FN (mean 3.36%), NE-AES (mean 3.23%), and WY–TGE (mean 1.97%). LTNA/D porosity is slightly higher than the helium porosity. The relatively low porosity of NE-AES corresponds to limited pore development observed in SEM images (Fig. 5(g)–(h)). The GL-QSK shales also exhibit the highest LTNA/D porosity, ranging from 8.17% to 10.69%, with an average of 9.50%, whereas the NE-AES shales have the lowest, with a mean of 2.86% (0.99%–4.91%). Notably, the LTNA/D porosity of the WY-TGE shales is significantly higher than their helium porosity, with average values of 4.53% and 1.97%, respectively.

3.3. NMR T_2 porosity

After removing the signals from the dry state, the NMR T_2 spectrum at the oil-saturated state represents the response of fluids within the shale pore networks. The NMR T_2 spectra at the oil-saturated state for the studied shales are shown in Fig. 7. Generally, three peaks are identified in the T_2 spectra, labeled as p1, p2, and p3, with the T_2 increasing, primarily corresponding to the micropores, mesopores, and macropores, respectively (Zhang et al., 2018). The moderate p1, large p2, and small p3 are the main features of the T_2 spectra of the GY-FN shales (Fig. 7(a)). The T_2 spectra of the AN-TGE shales are dominated by p2, with minimal p1 and p3, suggesting a predominance of mesopores in the AN-TGE shales (Fig. 7(b)). The T_2 spectra of NE-AES shales have diverse morphologies, mainly consisting of p1 and p2, as displayed in Fig. 7(c). The studied shales in the Wuliyasitai Sag have the most significant p1 but small p2 and p3 in the T_2 spectra, and the T_2 spectra of the WY-AES shales exhibit a smaller p2 peak compared to those of the WY-TGE shales (Fig. 7(d)–(e)). This means that the studied shales from the Wuliyasitai Sag primarily develop micropores. The T_2 spectra of the GL-QSK shales show spectral features similar to those of the GY-FN shales (Fig. 7(f)), but with a more prominent p1 peak, indicating a higher abundance of micropores.

Theoretically, the amplitude of the NMR T_2 spectrum is proportional to the pore volume. Thus, NMR T_2 porosity can be calculated by subtracting the amplitude at the dry state from that at the oil-saturated state. As demonstrated in Fig. 8(a), the NMR T_2 spectrum that refers to the pore fluid can be ascertained by comparing the T_2 spectra at the oil-saturated and dry states (Zhang et al., 2022; Li et al., 2023). As a result, excellent positive correlations occur between the pore oil volume and amplitude in the selected shales (Fig. 8(b)). The calibration coefficients relating amplitude to pore oil volume are summarized in Table 1, with all correlation coefficients exceeding 0.94, indicating the high reliability and accuracy of the NMR measurements.

However, variations in calibration coefficients are observed, primarily due to differences in mineral compositions among shales from different formations and sags. According to Eq. (2), the NMR T_2 porosity (φ_{N1}) can be derived, and the oil-saturated wetting porosity (φ_{ow}) can also be calculated based on Eq. (6). Theoretically, NMR T_2 porosity should align with oil-saturated wetting porosity, as both are indicative of the fluid-saturated content within shales. Thus, the relationship between T_2 and oil-saturated wetting porosity can refer to the accuracy of the NMR tests and reliable calibration coefficients. As shown in Fig. 9(a), T_2 porosity agrees well with oil-saturated wetting porosity, which justifies focusing on NMR T_2 porosity for further discussion. NMR T_2 porosity of the studied shales is exhibited in Fig. 9(b). The GL-QSK shales have the largest values, ranging from 8.59% to 14.75%, with a mean of 10.33%, followed by WY-AES (mean 7.39%), WY-TGE (mean 6.94%), AN-TGE (mean 5.17%), and GY-FN (mean 5.06%) shales. In contrast, the NE-AES shales have the lowest NMR T_2 porosity, spanning from 0.18% to 8.98%, with an average of 2.24%.

3.4. NMR T_1–T_2 porosity

Two-dimensional NMR T_1–T_2 is an innovative technique that comprehensively characterizes the pore fluid types (oil, water, or gas), contents, and occurrence states in shales (Li et al., 2018; Liu et al., 2022; Zhang et al., 2023). Previous studies indicate that porosity can be well determined by NMR T_1–T_2 based on the pressure coring shales (Li J.L. et al., 2024). However, the pressure-cored shales were sporadic. Thus, this study focuses on the shales after water and oil restoration (Fig. 10) (Zhang et al., 2024a, 2024b). The NMR T_1–T_2 spectrum can effectively disclose the pore fluid

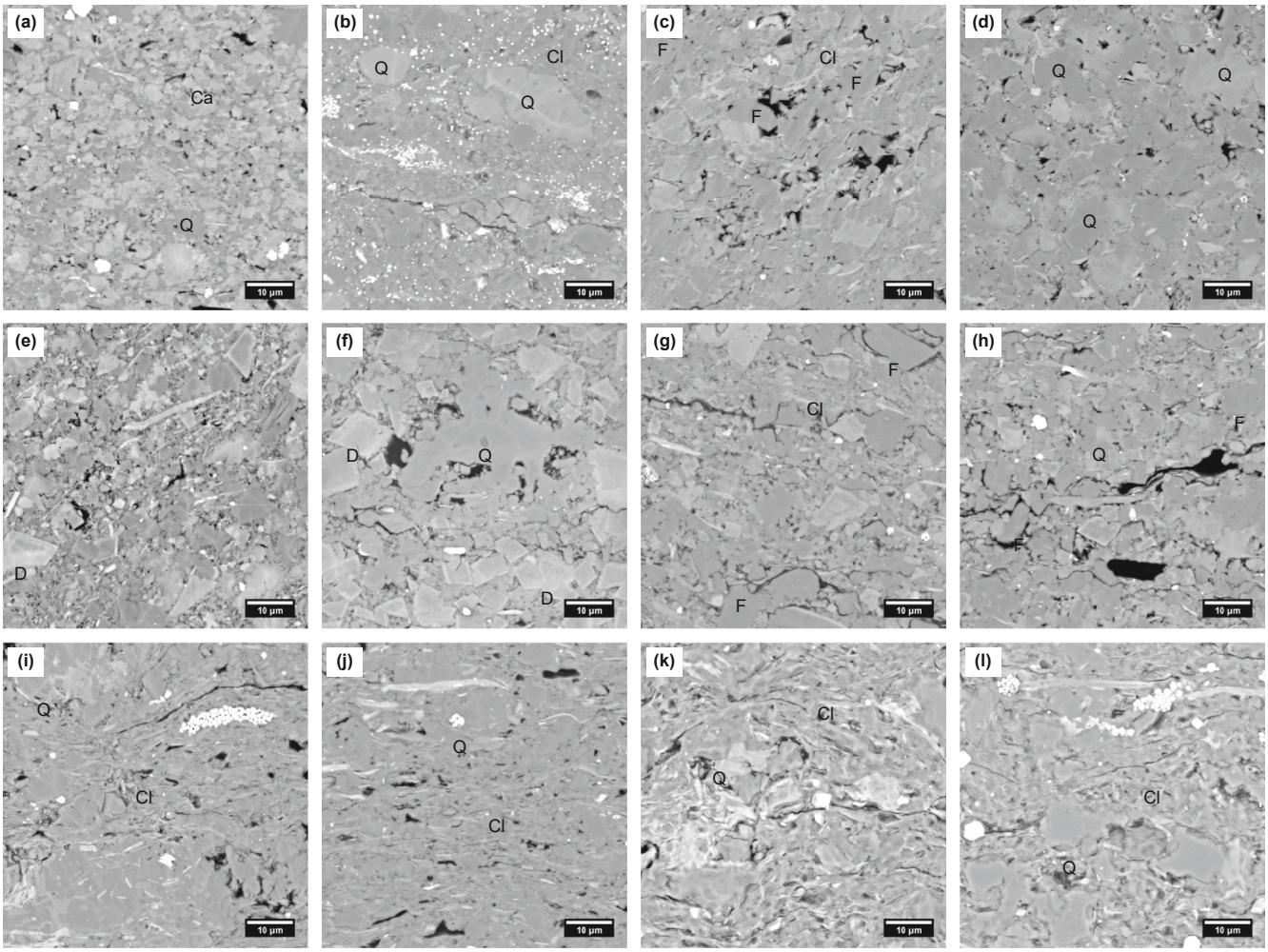

Fig. 5. SEM images of selected shales in different sags. **(a)** Gaoyou Sag, argillaceous-calcareous mixed shale, interparticle pores between or at the edges of carbonate minerals; **(b)** Gaoyou Sag, felsic-argillaceous mixed shale, intraparticle pores in clay mineral aggregates and interparticle pores edges of felsic minerals; **(c)** A'nan Sag, felsic-calcareous mixed shale, interparticle pores between or at the edges of granules; **(d)** A'nan Sag, carbonate-bearing argillaceous felsic-rich shale, interparticle pores between or at the edges of granules; **(e)** A'nan Sag, felsic-rich shale, interparticle pores between or at the edges of granules; **(f)** A'nan Sag, clay-bearing calcareous felsic-rich shale, interparticle pores; **(g)** Erennaoer Sag, clay-bearing calcareous felsic-rich shale, interparticle pores between or at the edges of granules; **(h)** Erennaoer Sag, felsic-calcareous mixed shale, interparticle pores between or at the edges of granules; **(i)** and **(j)** Wuliyasitai, carbonate-bearing felsic argillaceous-rich shale, intraparticle pores in clay mineral aggregates; **(k)** and **(l)** Gulong Sag, carbonate-bearing argillaceous felsic-rich shale, intraparticle pores in clay mineral aggregates.

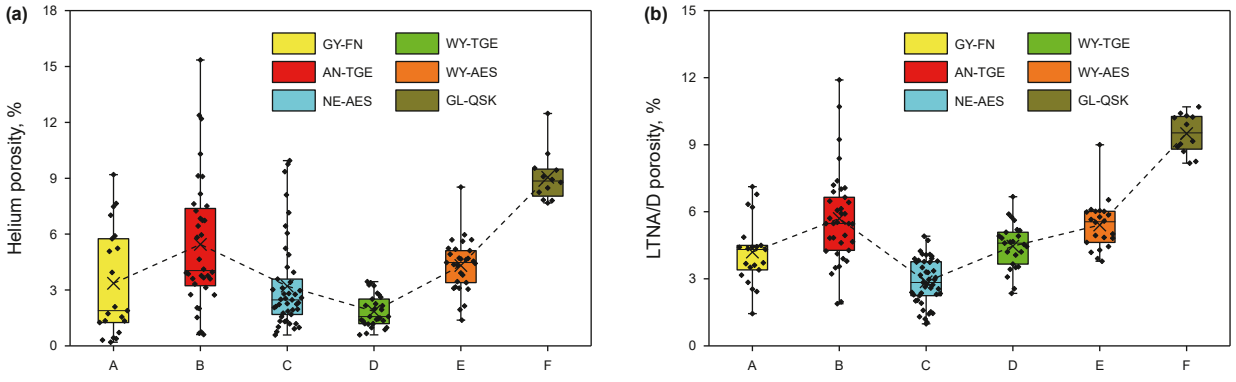

Fig. 6. Helium **(a)** and LTNA/D **(b)** porosity of the selected shales.

distributions in shale oil reservoirs, as shown in Fig. 10(a). According to the previous studies (Wang et al., 2024; Zhang et al., 2024a, 2024b), NMR T_1–T_2 spectrum can be clustered into eight regions (Fig. 10(a)). Regions A to E refer to the pore fluids, i.e., capillary-bound water, adsorbed oil, capillary-bound oil, movable oil, and movable water, respectively, while regions F to H denote the (quasi-) solid protons, such as clay-bound water, bitumen, and kerogen, respectively. According to Eqs. (3)–(5), the NMR T_1–T_2

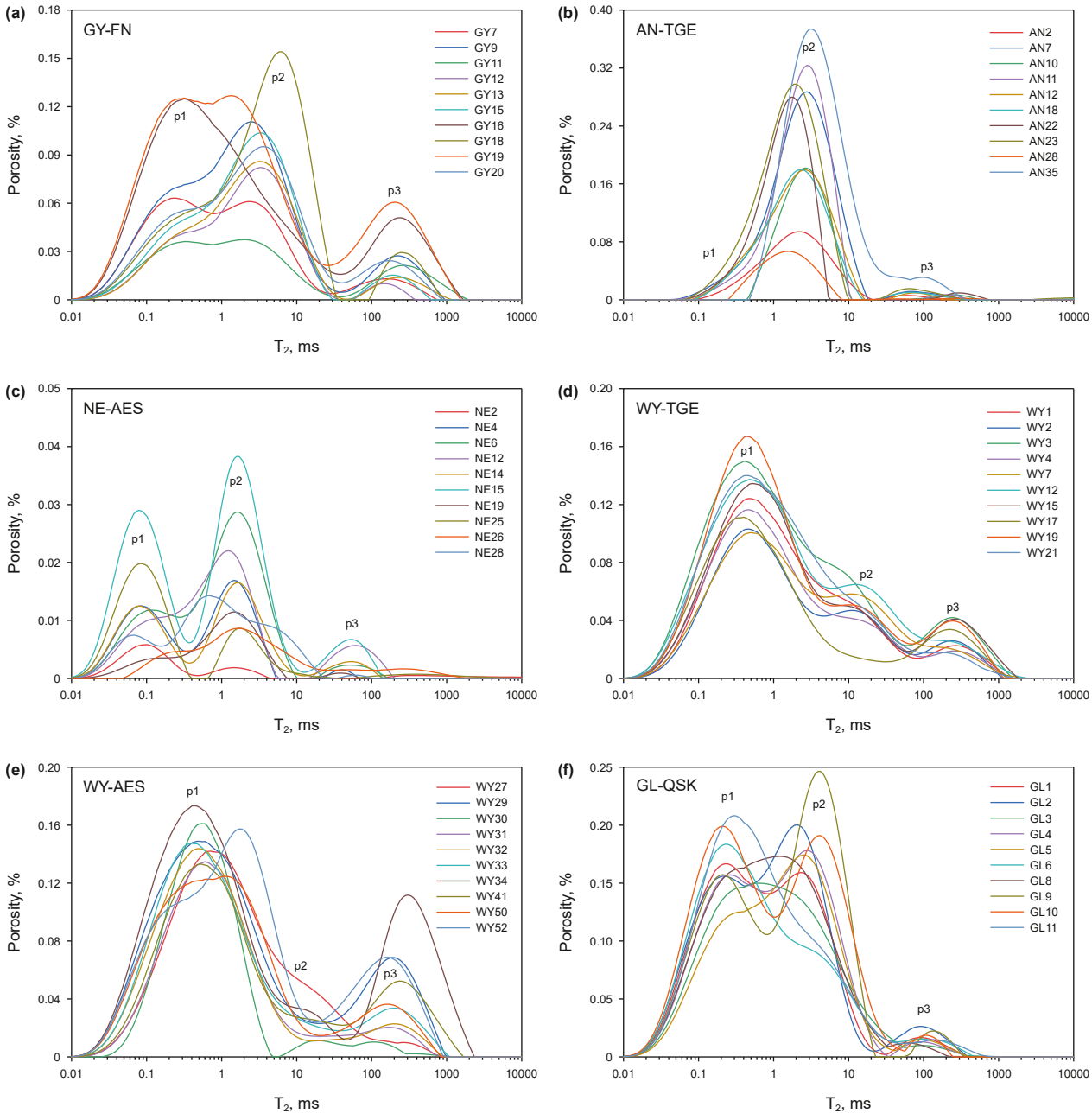

Fig. 7. NMR T_2 spectra of shales at the oil-saturated state from different sags.

porosity can be calculated based on the amplitudes of pore oil and water in the T_1–T_2 spectrum (Xiang et al., 2024). However, a critical step is to determine the calibration coefficients for the pore oil and water amplitudes in the T_1–T_2 spectrum.

The theoretical basis of NMR amplitude is that the amplitude of the NMR signal is directly proportional to the number of protons in the pore fluid. This relationship implies that the amplitude of the T_1–T_2 spectrum should be consistent with that of the T_2 spectrum for the same volume of oil or water, provided that the NMR test parameters are kept constant. Under this assumption, the calibration coefficient derived from the T_2 spectrum can be employed to calibrate the T_1–T_2 spectrum. This study compared the amplitudes of T_2 and T_1–T_2 spectra at the oil-saturated state. The T_1–T_2 spectra of the selected shales are shown in Fig. 10(b); adsorbed, capillary-bound, and movable oil can be identified according to the T_2 and T_1/T_2 values. The amplitude of the pore oil is the sum of the adsorbed, capillary-bound, and movable oil amplitudes. The relationships of amplitudes between T_2 and T_1–T_2 spectra at the oil-saturated state are plotted in Fig. 11. Excellent positive correlations are observed, suggesting that the amplitude of the T_1–T_2 spectrum is consistent with that of the T_2 spectrum.

Unfortunately, the amplitude of the T_1–T_2 spectrum is commonly lower than that of the T_2 spectrum. This discrepancy is more pronounced in shales with higher TOC. For instance, as shown in Fig. 11, the T_1–T_2 spectral amplitudes are in good agreement with the T_2 spectra amplitudes for AN-TGE shales, whereas the amplitudes of the T_2 spectra are consistently larger than those of the T_1–T_2 spectra for GL-QSK shales. The reason can be explained as follows. The T_2 spectra amplitude at the oil-saturated state encompasses all the oil saturated in shales, including

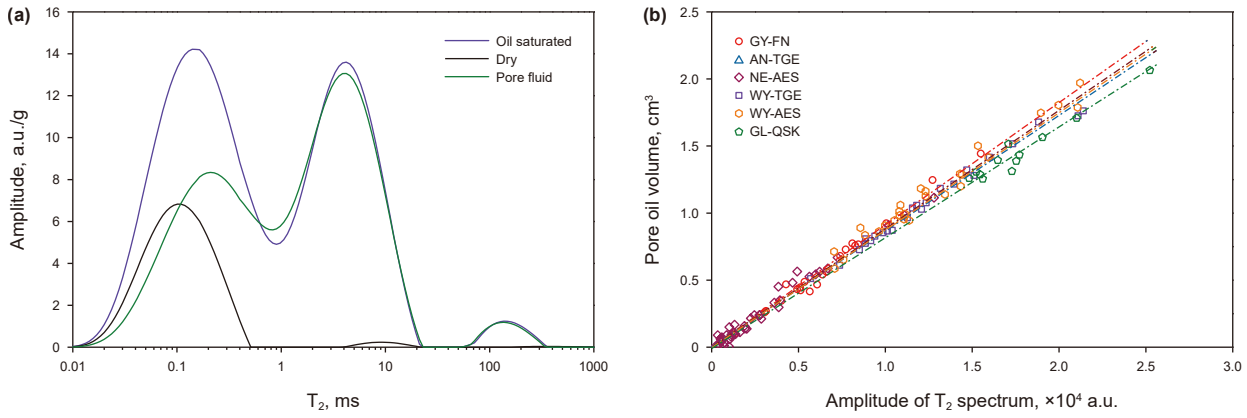

Fig. 8. NMR T_2 spectrum determination for pore fluid **(a)** and pore oil amplitude calibrations **(b)** in different sags.

Table 1
Calibration coefficients of pore oil and water in different sags.

Sag	Formation	Pore oil calibration		Pore water calibration	
		k_o	R^2	k_w	R^2
Gaoyou	Funing	0.9193	0.9799	0.5996	0.9358
A'nan	Tengger	0.8670	0.9803	0.8659	0.9608
Erennaoer	Aershan	0.9021	0.9793	0.7862	0.9111
Wuliyasitai	Tengger Aershan	0.8859	0.9724	0.5991	0.9367
Gulong	Qingshankou	0.8216	0.9422	0.7173	0.9793

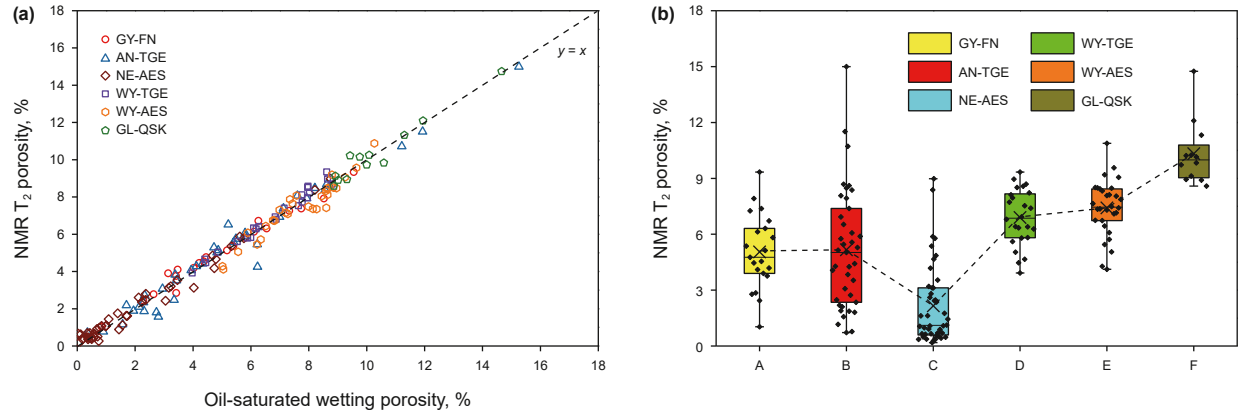

Fig. 9. Relationship between oil-saturated wetting and NMR T_2 porosity **(a)**, and NMR T_2 porosity distributions in different sags **(b)**.

the pore oil and the oil absorbed in organic matter. In contrast, the T_1–T_2 spectral amplitude only represents the pore oil. This is because the amplitude of the oil absorbed in organic matter occurs in regions G or H. As a result, the T_1–T_2 spectral amplitude is generally lower than the T_2 spectral amplitude. Given these observations, using the calibration coefficient determined by the T_2 spectrum may be a more accurate way to calibrate the T_1–T_2 spectrum.

The NMR amplitude calibration coefficient of pore water can be ascertained by comparing the T_2 spectral amplitudes and qualities at the as-received and water restoration states. The correlations between T_2 spectral amplitudes and pore water volumes in different sags are delineated in Fig. 12(a), demonstrating a strong positive correlation, with high correlation coefficients listed in Table 1. An interesting observation emerges from the results: the calibration coefficients for pore water vary markedly among different sags, whereas those for pore oil are relatively consistent. This discrepancy is primarily attributed to the influence of clay minerals: higher clay mineral content is generally associated with lower calibration coefficients for pore water.

According to the calibration coefficients for pore oil and water, the NMR T_1–T_2 porosity can be derived from the T_1–T_2 spectrum at water and oil restoration state, as depicted in Fig. 12(b). The NMR T_1–T_2 porosity shows strong agreement with NMR T_2 porosity (Figs. 9(b) and 12(b)). The GL-QSK shales are distinguished by the largest values, with an average of 10.10% (7.85%–15.38%), while the lowest values occur in the NE-AES shales, ranging from 1.25% to 9.99% (mean 3.24%). Additionally, the average NMR T_1–T_2 porosity values for GY-FN, AN-TGE, WY-TGE, and WY-AES are 6.30%, 6.25%, 6.47%, and 7.46%, respectively.

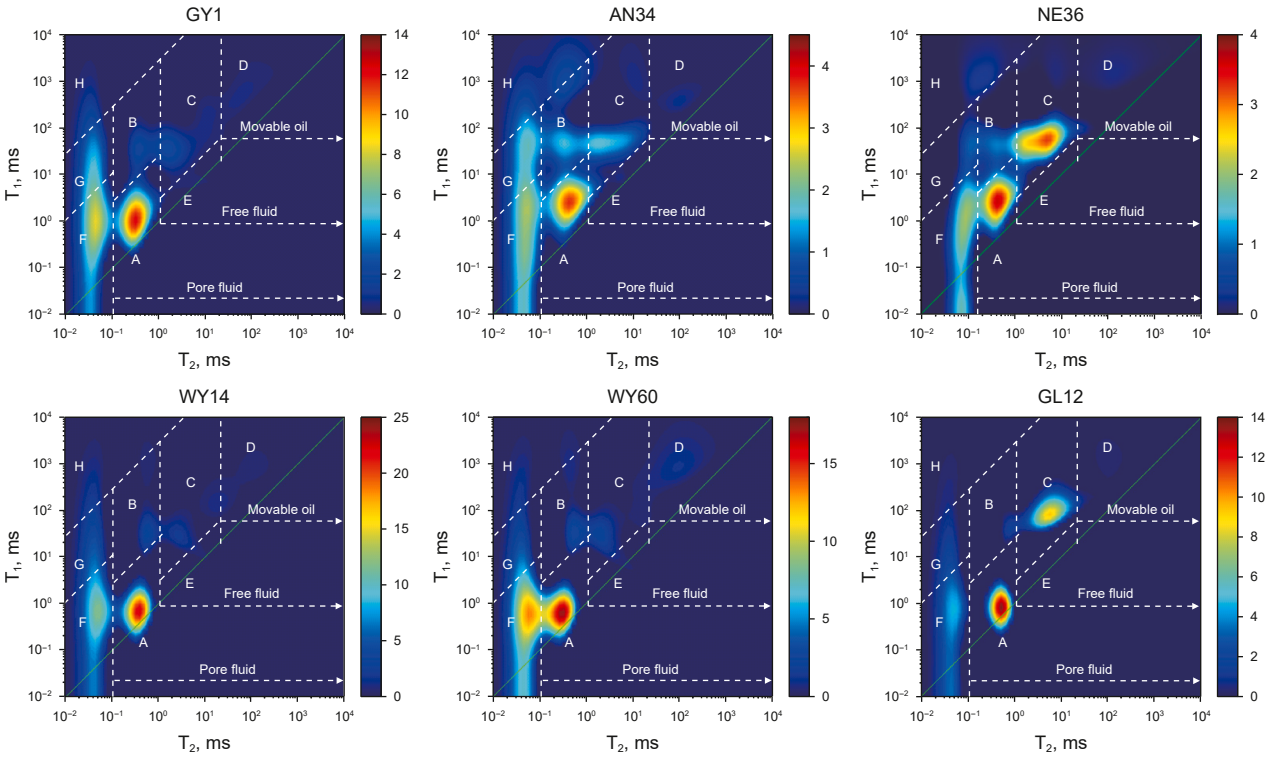

(a) T_1–T_2 spectra at water and oil restoration state

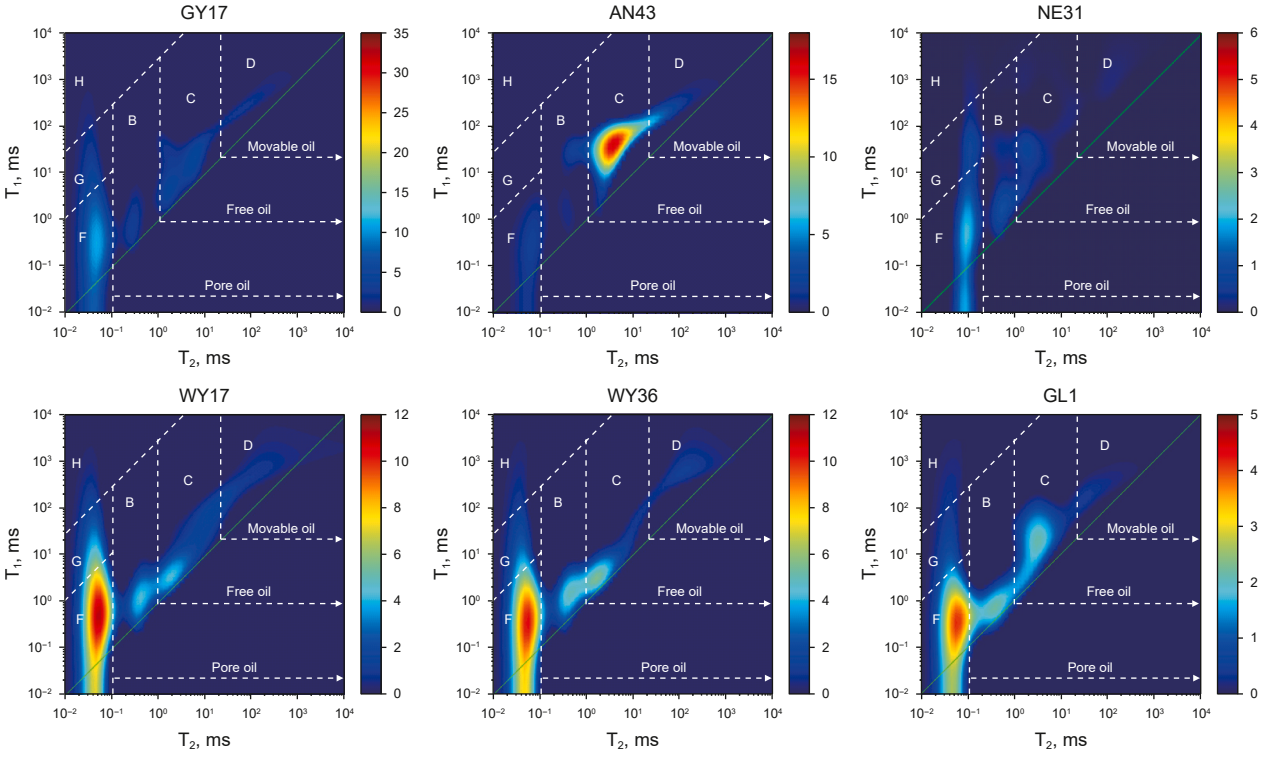

(b) T_1–T_2 spectra at oil-saturated state

Fig. 10. NMR T_1–T_2 spectra of shales at water and oil restoration **(a)** and oil-saturated **(b)** states. A, B, C, D, and E refer to capillary-bound water, adsorbed oil, capillary-bound oil, movable oil, and movable water; F, G, and H represent clay-bound water, bitumen, and kerogen, respectively.

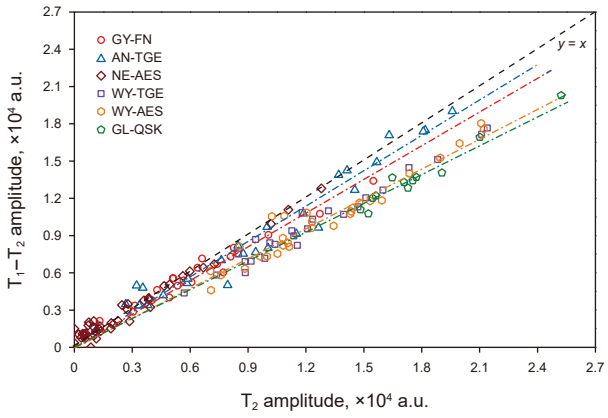

Fig. 11. Comparison between pore oil amplitudes in T_2 and T_1–T_2 spectra at the oil-saturated state in different sags.

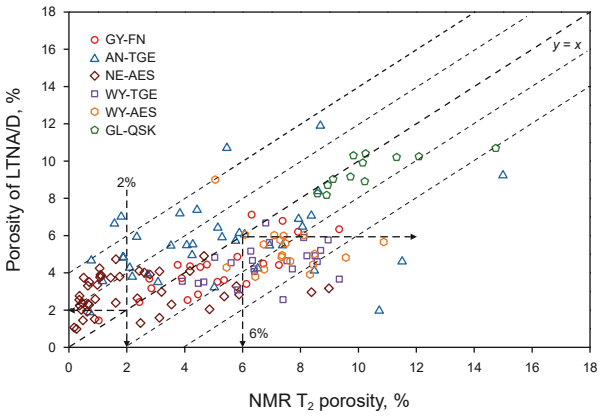

Fig. 13. Relationships between LTNA/D and NMR T_2 porosity.

4. Discussion

To determine the optimal testing method for shale porosity, LTNA/D, helium, and NMR T_1–T_2 porosity are compared with NMR T_2 porosity, as discussed in the following sections.

4.1. Comparison of LTNA/D and NMR T_2 porosity

The cross-plot between LTNA/D and NMR T_2 porosity is shown in Fig. 13. There are no obvious correlations between LTNA/D and NMR T_2 porosity in the selected samples. If the pores in shales are underdeveloped and mainly dominated by micropores, the LTNA/D porosity is typically larger than the T_2 porosity, as observed in the NE-AES shales with the T_2 porosity less than 2% (Fig. 5(g)–(h)). On the contrary, the T_2 porosity is generally larger than LTNA/D porosity when shales exhibit high porosity and a significant presence of meso- and macropores, such as the AN-TGE shales, which have T_2 porosity exceeding 6%. These observations may be explained by the following factors: crushing shale samples connects more micropores (Wang and Ju, 2015), which increases LTNA/D porosity, while LTNA/D mainly detects pores smaller than 200 nm (Zargari et al., 2015; Abelly et al., 2024). Consequently, many meso- and macropores may remain undetected, leading to a lower LTNA/D porosity. Therefore, due to the powder sample analysis and limited detection pore sizes, LTNA/D is not considered a suitable porosity testing method for shale oil reservoirs.

4.2. Comparison of helium and NMR T_2 porosity

The correlations between helium and NMR T_2 porosity are drawn in Fig. 14. Within the scope of this study, tight sandstone samples from the Jurassic Badaowan Formation in the Junggar Basin were utilized to substantiate the accuracy of both helium and T_2 porosity measurements. The helium porosity is consistent with T_2 porosity for the tight sandstone reservoirs. Unfortunately, a clear consistency between helium and T_2 porosity is not observed for the selected shales except for the AN-TGE shales. The helium porosity correlates well with T_2 porosity for AN-TGE shales, as evidenced by data points distributed on both sides of the diagonal line ($y = x$) in the cross-plot. A larger porosity commonly corresponds to a better consistency. However, a concerning phenomenon occurs: helium porosity is mainly larger than T_2 porosity for the NE-AES shales, particularly when the T_2 porosity is less than 2%. On the contrary, helium porosity is generally lower than T_2 porosity for the GY-FN, WY-TGE, WY-AES, and GL-QSK shales.

Several hypotheses have been posited to elucidate these phenomena. In samples with low clay mineral content and high porosity, such as in tight sandstones, both helium and T_2 porosity measurements can accurately ascertain the porosity levels. Conversely, in shales with low porosity and clay mineral content, helium gas penetrates smaller pores more readily than oil (specifically *n*-dodecane in this study), resulting in a larger helium porosity than T_2 porosity, such as NE-AES shales. However, if shale samples have a high content of clay minerals (more than 30%), the

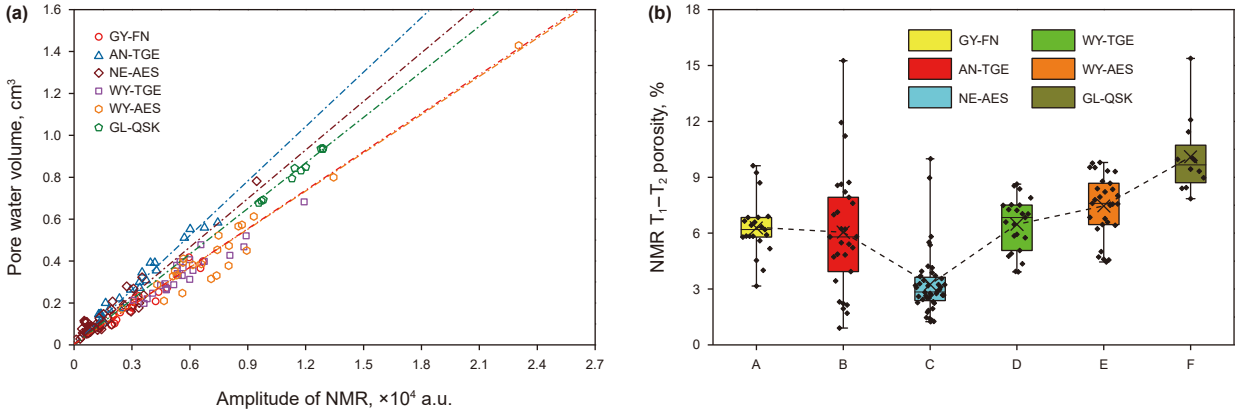

Fig. 12. NMR amplitude calibrations of pore water (**a**) and NMR T_1–T_2 porosity (**b**) in different sags.

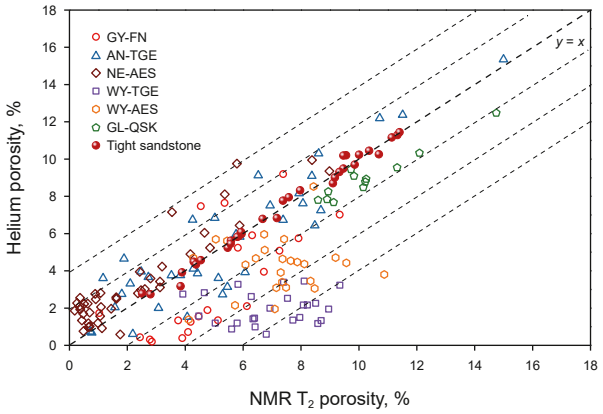

Fig. 14. Relationships between helium and NMR T_2 porosity.

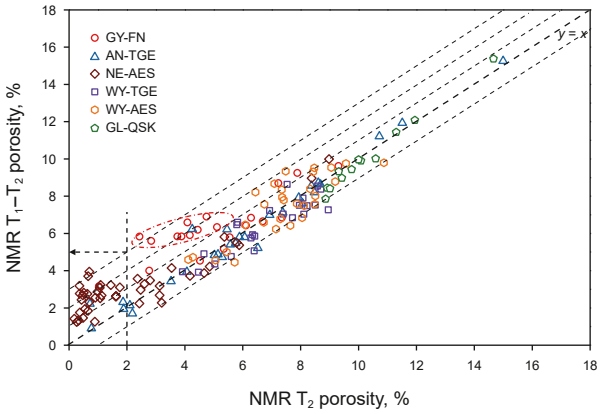

Fig. 15. Relationships between NMR T_2 and T_1–T_2 porosity.

pore system is more intricate, requiring longer equilibration times for helium to fully saturate the pore network. According to the principle of helium porosity measurements (Xue et al., 2017), insufficient equilibration results in an overestimation of the solid skeleton volume and a corresponding underestimation of the pore volume, thereby yielding lower helium porosity values.

Therefore, if the equilibrium duration is insufficient, helium porosity measurements will be underestimated. A higher clay mineral content corresponds to a more complex pore structure, resulting in helium porosity values that are lower than T_2 porosity. As a result, shale oil reservoirs in the Wuliyasitai Sag, mainly consisting of carbonate-bearing felsic argillaceous-rich shales, are characterized by much lower helium porosity compared with T_2 porosity. This trend is also evident in GY-FN and GL-QSK shales, with average clay mineral contents surpassing 30%. Therefore, it can be inferred that sufficient equilibrium time is essential for accurate helium porosity assessments, and an underestimated porosity may be obtained if an insufficient equilibrium time is adopted.

4.3. Comparison of NMR T_1–T_2 and T_2 porosity

Compared to LTNA/D and helium porosity, a superior level of correlation is observed between NMR T_1–T_2 and T_2 porosity, as demonstrated in Fig. 15. The T_1–T_2 porosity closely aligns with T_2 porosity for AN-TGE, WY-TGE, WY-AES, and GL-QSK shales, with the discrepancies generally not exceeding 1%. This suggests that both NMR T_1–T_2 and T_2 porosity can effectively evaluate the porosity of shale oil reservoirs. Surprisingly, the T_1–T_2 porosity of NE-AES shales is generally larger than the T_2 porosity, especially for the shales with T_2 porosity less than 2%. The rationale behind this discrepancy may be attributed to the following: The T_1–T_2 porosity is obtained based on the T_1–T_2 spectrum at water and oil restoration state, whereas the T_2 porosity is ascertained by comparing the T_2 spectra at the oil-saturated and dry states.

Thus, if residual oil in the shale pore system is not entirely eliminated through the washing and drying processes, the T_2 spectrum at the dry state will include minor fluid responses, leading to a diminished amplitude of the T_2 spectrum at the oil-saturated state after subtracting T_2 response at dry state (Li et al., 2019, 2024). Correspondingly, the T_1–T_2 porosity will be larger than the T_2 porosity. Take NE-AES shale as a case in point; the incapability to fully remove residual oil due to its extremely low porosity and intricate pore structure is corroborated by the T_1–T_2 spectra at the dry state, as displayed in Fig. 16(a)–(c). Slight amplitudes associated with capillary-bound water, adsorbed, and capillary-bound oil can be identified in regions A, B, and C. However, AN-TGE, WY-TGE, and GL-QSK shales exhibit nearly negligible amplitudes, as exhibited in Fig. 16(e) and (f). Therefore, the NMR T_1–T_2 technique emerges as a viable alternative for accurately evaluating the porosity of shale oil reservoirs, especially for shales with low porosity and complex pore structure.

Additionally, the scenario where T_1–T_2 porosity exceeds T_2 porosity has also been discovered in the GY-FN shales (Fig. 15). This phenomenon may be attributed to the microstructural characteristics of clay mineral aggregates. As shown in Fig. 17(a)–(d), few pores are identifiable within clay mineral aggregates in the GY-FN shales, in contrast to the abundant intraparticle pores associated with clay minerals in selected shales from the Wuliyashitai and Gulong sags (Fig. 17(e)–(h)). Consequently, intraparticle pores within clay mineral aggregates can be saturated with oil in the WY-TGE, WY-AES, and GL-QSK shales. In contrast, oil penetration into the tight clay mineral aggregates of GY-FN shales is challenging. However, since clay minerals are predominantly hydrophilic, these aggregates can readily be saturated with water. As a result, the T_1–T_2 porosity obtained at the water and oil restoration state is larger than the T_2 porosity obtained at the oil-saturated state for GY-FN shales. Therefore, T_1–T_2 porosity should be the total porosity, while T_2 porosity is the effective porosity.

4.4. Suggestions for porosity testing of shale oil reservoirs

This study discusses five techniques for detecting the porosity of shale oil reservoirs, including LTNA/D, helium porosity, oil-saturated wetting, NMR T_2, and T_1–T_2. Four distinct media were utilized to detect pores: helium, nitrogen, water, and *n*-dodecane. The molecular diameters of helium, nitrogen, and water are approximately 0.26, 0.364, and 0.4 nm, respectively. However, due to its long molecular chain, *n*-dodecane has a length and diameter of approximately 1.694 and 0.4 nm, respectively. Theoretically, the pore detection limits in ascending order correspond to helium, nitrogen, water, and *n*-dodecane. Nevertheless, LTNA/D primarily detects pores within the range of approximately 1.7–200 nm (Zargari et al., 2015; Abelly et al., 2024). Under dry conditions following vacuum treatment, nitrogen, water, and *n*-dodecane all act as wetting phases for shale pore surfaces, while helium behaves as a non-adsorbed gas. Consequently, the molecular diameter determines the pore detection limit rather than the test pressure. The advantages and influence factors of these techniques are summarized in Table 2.

LTNA/D, which is performed on powdered samples with more connected pores detected, is limited in its ability to detect pores

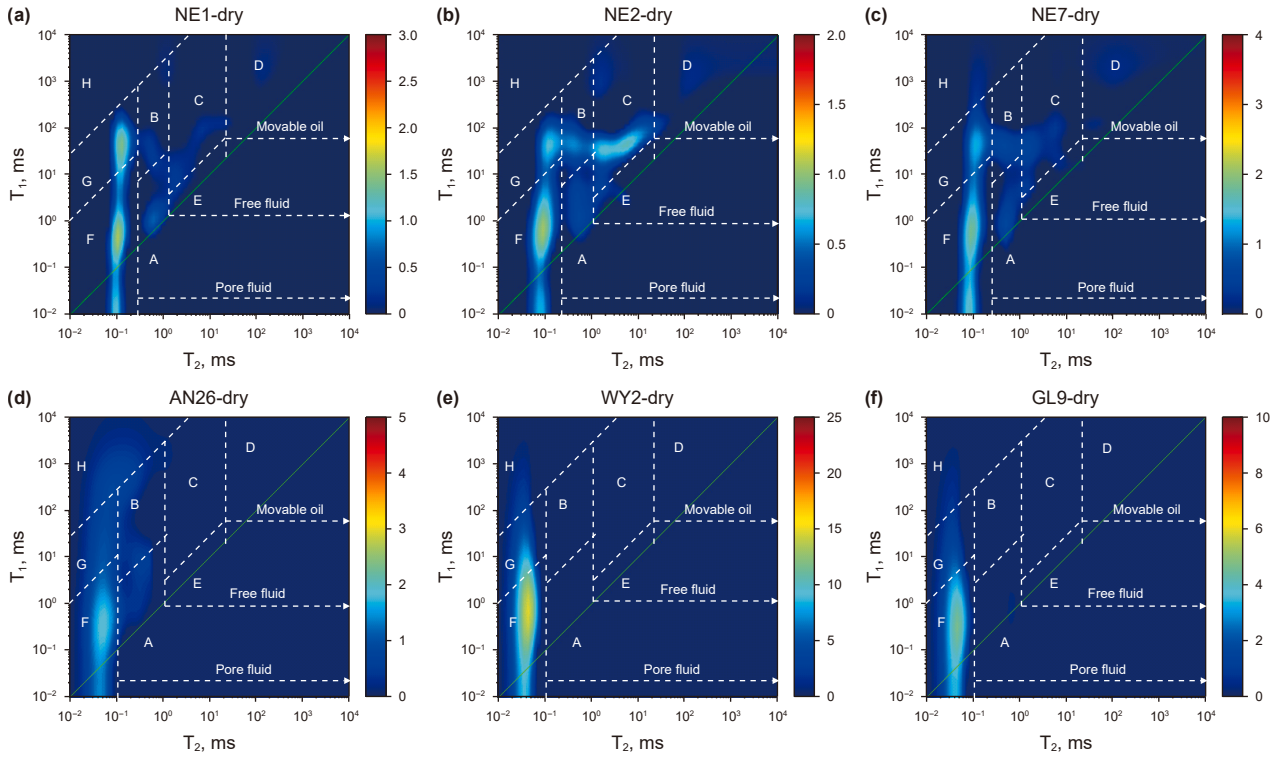

Fig. 16. NMR T_1–T_2 spectra of the dry samples from different sags. A, B, C, D, and E refer to capillary-bound water, adsorbed oil, capillary-bound oil, movable oil, and movable water; F, G, and H represent clay-bound water, bitumen, and kerogen, respectively.

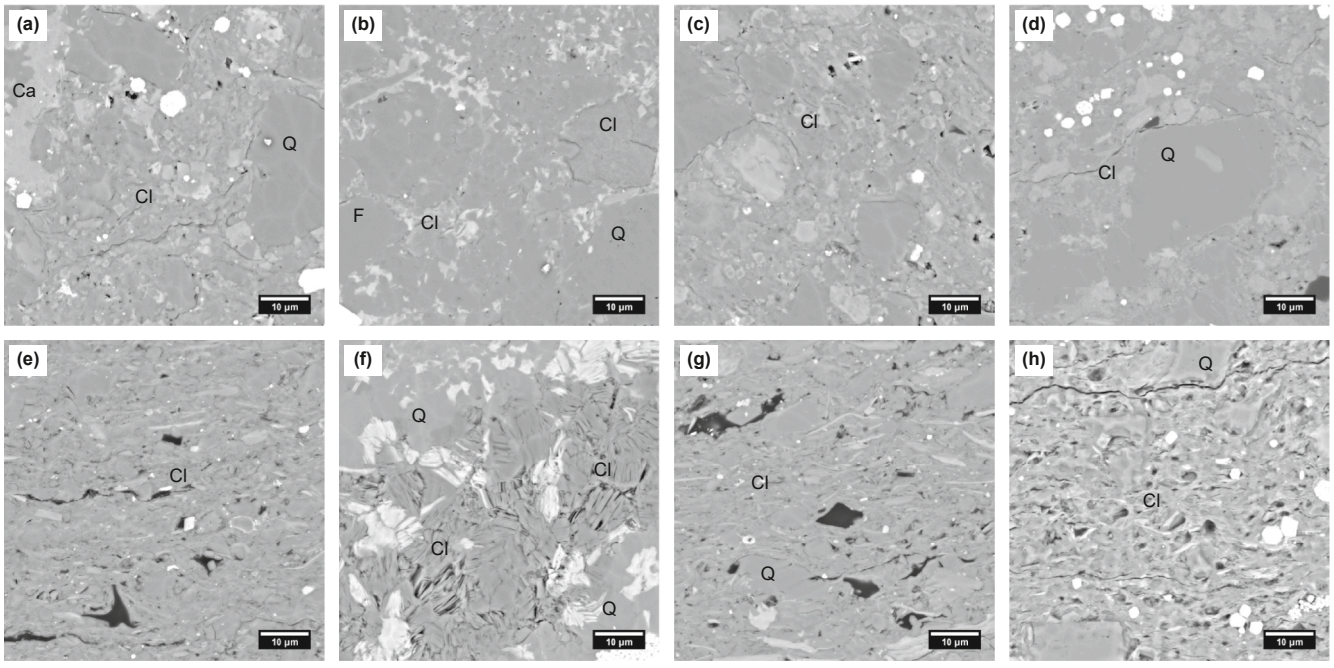

Fig. 17. Clay mineral characteristics in shales from different sags. **(a)**–**(d)** Refer to shales from the Gaoyou Sag; **(e)**–**(g)** denote shales from the Wuliyasitai Sag; **(h)** represents shales from the Gulong Sag.

larger than 200 nm. Consequently, LTNA/D is deemed unsuitable for evaluating the porosity of shale oil reservoirs, which is characterized by a multi-scale distribution of pore systems. Helium porosity is widely acknowledged as the premier method for detecting shale porosity, attributed to its minute molecular size and non-adsorptive nature (Clarkson et al., 2012). However, longer equilibrium times should be adopted for tight shales with complex pore structures. Insufficient equilibrium times may result in underestimating helium porosity (Fig. 14). Varying equilibrium durations should be tailored to shale samples from different basins

Table 2
Advantages and influence factors of LTNA/D, helium porosity, oil-saturated, NMR T_2, and T_1–T_2 in detecting shale porosity.

Methods	Detection range, nm	Advantages	Influence factors
Helium	>0.26	Minimum molecular diameter and non-adsorption	Equilibrium time; Residual pore fluids;
LTNA/D	~1.7–~200	More connected pores can be detected after crushing	Sample size; Detection range;
Oil-saturated	>0.4	Efficient and convenient	Residual pore fluids; Organic matter contents;
NMR T_2	>0.4	Non-destructive and efficient	Residual pore fluids; Organic matter contents; Test parameters;
NMR T_1–T_2	>0.4	Non-destructive and efficient; No need to remove residual fluids	Calibration coefficients; Test parameters

or lithologies. Thus, it is imperative to establish specific testing parameters and protocols for the targeted shale samples. Caution should be exercised when utilizing helium porosity to assess shale oil reservoirs. In addition, helium porosity is performed on the shale sample after washing the oil and drying. A lower helium porosity will be obtained if the residual pore fluids cannot be removed entirely.

NMR T_2 technique is an effective method for measuring the porosity of shale oil reservoirs, demonstrating excellent consistency with oil-saturated wetting porosity. The accuracy of the T_2 porosity is directly affected by the testing parameters (such as TE), process, and pretreatment (washing oil and drying, and saturation) (Hinai et al., 2014; Testamanti and Rezaee, 2019). Before the NMR tests, the shale samples should be washed, dried, and then saturated with light oil (such as *n*-dodecane). Higher pressure and longer time are necessary to saturate the shale pore system with oil. Porosity can be ascertained from the T_2 spectrum at the oil-saturated state after subtracting the amplitude detected at the dry state, which is measured at an extremely low TE (such as 0.07 ms) (Zhang et al., 2022; Xiang et al., 2024). However, residual fluids also affect NMR T_2 porosity. Moreover, organic matter has the capacity to adsorb a portion of the oil during the saturation process, which can result in an overestimation of NMR T_2 porosity (Li et al., 2023). A similar overestimation can also occur with oil-saturated wetting porosity. Consequently, in shales with high organic matter content, the porosity may be overestimated when using either the NMR T_2 or the oil-saturated wetting methods.

NMR T_1–T_2 technique offers an alternative and innovative approach to assessing the porosity of shale oil reservoirs. The NMR T_1–T_2 spectrum at water and oil restoration state can accurately reflect the total pore fluids within the shale pore systems, and porosity can be calculated post-calibration. As previously discussed, NMR T_1–T_2 porosity refers to the total porosity, while T_2 porosity represents the effective porosity. However, there are inherent limitations to this approach. Pore oil at water and oil restoration state is composed of light oil and some heavy components (Wang et al., 2022b; Lin et al., 2024). The application of calibration coefficients intended for light oil may, therefore, introduce inaccuracies in the volume calibration of oil. It is recommended that future studies establish calibration coefficients specific to pore oil using the actual crude oil samples (Li J.B. et al., 2024). In conclusion, NMR T_2 and T_1–T_2 techniques are recommended to characterize the porosity of shale oil reservoirs, while the application of helium porosity should be approached with caution. However, shale porosity is usually not accurately reflected by the LTNA/D method.

While this study focused on laboratory-based conditions, it should be acknowledged that in situ pore structures may be further affected by mechanical deformation and geochemical processes such as compaction, microfracturing, water-rock, and oil-rock interactions (Kozhevnikov et al., 2024; Zhao F.Z. et al., 2024; Xu et al., 2025). These factors could potentially influence porosity evolution and NMR responses in subsurface environments (Zhao L.L. et al., 2024). Future work should consider integrating these effects to enhance the applicability of NMR porosity characterization under reservoir conditions.

5. Conclusions

This study employed helium porosity, LTNA/D, NMR T_2 and T_1–T_2, and oil-saturated wetting methods to characterize the porosity of shale oil reservoirs. A critical analysis of the strengths and limitations of each method was conducted to ascertain the most appropriate techniques for porosity assessment in these reservoirs. The key findings are summarized below.

(1) The porosity originating from the LTNA/D on powdered samples presents challenges in accurately gauging the porosity of shales. Helium, with its minuscule molecular size and non-adsorptive properties, is deemed an optimal gas for probing shale pore systems. However, helium porosity is restricted by the equilibration time and the residual pore fluids after washing oil and drying. Insufficient equilibration can lead to underestimated helium porosity values. The residual pore fluids occupy a portion of the pore space, leading to a lower helium porosity for shale oil reservoirs. Helium porosity is more suitable for detecting the porosity of shale oil reservoirs with a low content of clay minerals.

(2) NMR T_2 porosity strongly correlates with oil-saturated wetting porosity, collectively reflecting the volume of pore fluids. The T_2 spectrum at the oil-saturated state, after subtracting the amplitude at the dry state, can accurately characterize shale porosity. However, NMR T_2 porosity may be underestimated if residual pore fluids persist within the shale pore systems post-oil washing and drying. Moreover, porosity may be overestimated if the shale has a high organic matter content.

(3) NMR T_1–T_2 spectrum provides an innovative technique for quantitatively evaluating pore fluid contents in shale oil reservoirs. Accurate shale porosity can be obtained from the T_1–T_2 spectrum at the water and oil restoration state. T_1–T_2 porosity generally exhibits good consistency with T_2 porosity. In cases where complete removal of residual pore fluids is challenging, the T_1–T_2 technique can more accurately determine shale porosity. Overall, T_1–T_2 porosity refers to the total porosity, while T_2 porosity represents the effective porosity.

(4) Test parameters are fundamental to NMR measurements, and the parameters employed in this study are recommended for adoption. However, the waiting time (TW), number of scans (NS), and echo number (NECH) should be

adjusted following the characteristics of shale pore structures. When shales contain a higher proportion of large pores and fractures, larger values of TW and NECH are required. Conversely, increasing the number of scans (NS) is advisable if the porosity is low. Notably, maintaining consistent test parameters is essential for a specific test analysis. Using actual crude oil samples to calibrate pore oil volume is recommended for future research.

CRediT authorship contribution statement

Jun-Jie Wang: Writing – original draft, Investigation, Funding acquisition. **Peng-Fei Zhang:** Writing – review & editing, Methodology, Funding acquisition, Data curation. **Shuang-Fang Lu:** Writing – review & editing, Methodology. **Wei-Zheng Gao:** Investigation. **Neng-Wu Zhou:** Methodology, Investigation. **Wen-Biao Li:** Writing – review & editing, Methodology. **Guo-Hui Chen:** Writing – review & editing, Methodology.

Declaration of competing interest

The authors declare that they have no known competing financial interests or personal relationships that could have appeared to influence the work reported in this paper.

Acknowledgments

This study was financially supported by the PhD Scientific Research and Innovation Foundation of the Education Department of Hainan Province Joint Project of Sanya Yazhou Bay Science and Technology City (HSPHDSRF202407-001), the Project of Sanya Yazhou Bay Science and Technology City (SCKJ-JYRC-2023-01), the National Natural Science Foundation of China (42302160), and Educational Reform of Hainan Higher Education Institutions (Hnjg2024-276).

References

Abelly, E.N., Yang, F., Ngata, M.R., Mwakipunda, G.C., Shanghvi, E.R., 2024. A field study of pore-network systems on the tight shale gas formation through adsorption-desorption technique and mercury intrusion capillary porosimeter: percolation theory and simulations. Energy 302, 131771. https://doi.org/10.1016/j.energy.2024.131771.

Bai, G.S., Chen, G.H., Cai, Z.X., Yan, H.X., Lu, S.F., Radwn, A.E., 2025. Movable oil content evaluation in low-to-medium maturity lacustrine shale during in-situ conversion. Adv. Geo-Energy Res. 16 (1), 77–90. https://doi.org/10.46690/ager.2025.04.08.

Bechtel, A., Jia, J.L., Strobl, S.A.I., Sachsenhofer, R.F., Liu, Z.J., Gratzer, R., Püttmannet, W., 2012. Palaeoenvironmental conditions during deposition of the Upper Cretaceous oil shale sequences in the Songliao Basin (NE China): Implications from geochemical analysis. Org. Geochem. 46, 76–95. https://doi.org/10.1016/j.orggeochem.2012.02.003.

Chen, C., Lu, S.F., Zhang, P.F., Li, J.Q., Li, W.B., Wang, S.Y., 2020. Key factors influencing the low-field NMR characterization of gas- and oil-bearing shales: A case study of the shales from the southern Sichuan Basin and Dongying Sag, China. Int. J. Oil Gas Coal Technol. 24, 466–482. https://doi.org/10.1504/IJOGCT.2020.108049.

Clarkson, C.R., Freeman, M., He, L., Agamalian, M., Melnichenko, Y.B., Mastalerz, M., Bustin, R.M., Radliński, A.P., Blach, T.P., 2012. Characterization of tight gas reservoir pore structure using USANS/SANS and gas adsorption analysis. Fuel 95, 371–385. https://doi.org/10.1016/j.fuel.2011.12.010.

Ding, X.J., Liu, G.D., Zha, M., Huang, Z.L., Gao, C.H., Wang, P.G., Qu, J.X., Lu, X.J., Chen, Z.L., 2015. Characteristics and origin of lacustrine source rocks in the Lower Cretaceous, Erlian Basin, Northern China. Mar. Petrol. Geol. 66, 939–955. https://doi.org/10.1016/j.marpetgeo.2015.08.002.

Ding, X.J., Liu, G.D., Zha, M., Gao, C.H., Huang, Z.L., Qu, J.X., Lu, X.J., Wang, P.G., Chen, Z.L., 2016. Geochemical characterization and depositional environment of source rocks of small fault basin in Erlian Basin, Northern China. Mar. Petrol. Geol. 69, 231–240. https://doi.org/10.1016/j.marpetgeo.2015.11.006.

Elsayed, M., Iash, A., Hiba, M., Hassan, A., Ai-Garadi, K., Mahmoud, M., El-Husseiny, A., Radwan, A.E., 2022. A review on the applications of nuclear magnetic resonance (NMR) in the oil and gas industry: Laboratory and field-scale measurements. J. Pet. Explor. Prod. Technol. 12, 2747–2784. https://doi.org/10.1007/s13202-022-01476-3.

Fan, Q.Z., Cheng, P., Tian, H., Gai, H.F., Xiao, X.M., 2023. Distribution and occurrence of pore water and retained oil in nanopores of marine-terrestrial transitional shales during oil generation and expulsion: Implications from a thermal simulation experiment on shale plug samples. Mar. Petrol. Geol. 150, 106125. https://doi.org/10.1016/j.marpetgeo.2023.106125.

Fan, X.J., Lu, Y.B., Liu, Z.H., Lu, Y.C., Zhang, J.Y., Deng, K., Zhu, T., Tai, H., Li, L., 2024. Lacustrine shale lithofacies and depositional environment in the Paleocene Second Member of the Funing Formation, Subei Basin, China: Insights into shale oil development prospects. Mar. Petrol. Geol. 164, 106849. https://doi.org/10.1016/j.marpetgeo.2024.106849.

Fleury, M., Romero-Sarmiento, M., 2016. Characterization of shales using T_1–T_2 NMR maps. J. Petrol. Sci. Eng. 137, 56–62. https://doi.org/10.1016/j.petrol.2015.11.006.

Fu, Q., Hu, Z.Q., Feng, D.J., Huang, J.L., Xing, L.L., Zhu, Z.W., Teng, W., 2023. Restoration and evolution of the Paleogene (E_1f_2) shale sedimentary environment in the Subei Basin, China. ACS Omega 8, 46892–46903. https://doi.org/10.1021/acsomega.3c06603.

Habina, I., Radzik, N., Topór, T., Krzyżak, A.T., 2017. Insight into oil and gas-shales compounds signatures in low field ^{1}H NMR and its application in porosity evaluation. Microporous Mesoporous Mater. 252, 37–49. https://doi.org/10.1016/j.micromeso.2017.05.054.

Hinai, A.A., Rezaee, R., Esteban, L., Labani, M., 2014. Comparisons of pore size distribution: A case from the Western Australian gas shale formations. J. Unconv. Oil Gas Res. 8, 1–13. https://doi.org/10.1016/j.juogr.2014.06.002.

Hu, Q.H., Zhang, X.Y., Meng, X.H., Li, Z., Xie, Z.H., Lin, M.W., 2017. Characterization of micro-nano pore networks in shale oil reservoirs of Paleogene Shahejie formation in Dongying Sag of Bohai Bay Basin, East China. Petrol. Explor. Dev. 44, 681–690. https://doi.org/10.11698/PED.2017.05.03.

Jarvie, D.M., 2012. Shale resource systems for oil and gas; part 2, shale-oil resource systems. AAPG Mem. 9, 89–119. https://doi.org/10.1306/13321447M973489.

Kozhevnikov, E., Turbakov, M., Riabokon, E., Gladkikh, E., Guzev, M., Qi, C.Z., Li, X.Z., 2024. The mechanism of porous reservoir permeability deterioration due to pore pressure decrease. Adv. Geo-Energy Res. 13 (2), 96–105. https://doi.org/10.46690/ager.2024.08.04.

Li, J.B., Huang, W.B., Lu, S.F., Wang, M., Chen, G.H., Tian, W.C., Guo, Z.Q., 2018. Nuclear magnetic resonance T_1–T_2 map division method for hydrogen-bearing components in Continental shale. Energy Fuel. 32, 9043–9054. https://doi.org/10.1021/acs.energyfuels.8b01541.

Li, J.B., Lu, S.F., Chen, G.H., Wang, M., Tian, S.S., Guo, Z.Q., 2019. A new method for measuring shale porosity with low-field nuclear magnetic resonance considering non-fluid signals. Mar. Petrol. Geol. 102, 535–543. https://doi.org/10.1016/j.marpetgeo.2019.01.013.

Li, J.B., Wang, M., Fei, J.S., Xu, L., Shao, H.M., Li, M., Tian, W.C., Lu, S.F., 2022. Determination of *in situ* hydrocarbon contents in shale oil plays. Part 2: Two-dimensional nuclear magnetic resonance (2D NMR) as a potential approach to characterize preserved cores. Mar. Petrol. Geol. 145, 105890. https://doi.org/10.1016/j.marpetgeo.2022.105890.

Li, J.B., Wang, M., Shao, H.M., Li, M., Liu, L., Lu, S.F., 2023. Shale porosity measurement by the saturated oil method: Removing the contribution from oils dissolved in kerogen. Pet. Sci. 20, 3273–3279. https://doi.org/10.1016/j.petsci.2023.07.006.

Li, J.L., Wang, M., Wang, M., Li, J.B., Zhao, X.B., Hu, X.Z., Fu, A.B., 2024. Shale primary porosimetry based on 2D nuclear magnetic resonance of T_1-T_2. Energy Geosci. 5, 100270. https://doi.org/10.1016/j.engeos.2023.100270.

Li, W.B., Wang, J., Jia, C.Z., Lu, S.F., Li, J.Q., Zhang, P.F., Wei, Y.B., Song, Z.J., Chen, G.H., Zhou, N.W., 2024. Carbon isotope fractionation during methane transport through tight sedimentary rocks: Phenomena, mechanisms, characterization, and implications. Geosci. Front. 15, 101912. https://doi.org/10.1016/j.gsf.2024.101912.

Lin, Z.Z., Li, J.Q., Lu, S.F., Hu, Q.H., Zhang, P.F., Wang, J.J., Zhi, Q., Huang, H.S., Yin, N., Wang, Y., Ge, T.C., 2024. The occurrence characteristics of oil in shales matrix from organic geochemical screening data and pore structure properties: An experimental study. Pet. Sci. 21 (1), 1–13. https://doi.org/10.1016/j.petsci.2023.09.002.

Liu, B., Jiang, X.W., Bai, L.H., Lu, R.S., 2022. Investigation of oil and water migrations in lacustrine oil shales using 20 MHz 2D NMR relaxometry techniques. Pet. Sci. 19 (3), 1007–1018. https://doi.org/10.1016/j.petsci.2021.10.011.

Liu, H., Liu, X.P., Liu, G.Y., Li, G.Y., Wang, J.W., Gao, Y.L., Sun, B., Hou, J.K., Liu, H.X., Sun, X.J., 2023. Sedimentary environment controls on the lacustrine shale lithofacies: A case study from the Nanpu depression, Bohai Bay Basin. Geoenergy Sci. Eng. 225, 211704. https://doi.org/10.1016/j.geoen.2023.211704.

Ma, X.X., Hou, D.J., Wu, P., Cheng, X., Ding, W.J., Cao, L.Z., Wei, X.L., Zheng, R.H., 2023. Organic geochemistry and organic matter enrichment mechanisms of the lacustrine source rocks from a small-faulted Basin: A case study of the Bayindulan, A'er and Wuliyasitai sags in the Erlian Basin, Northern China. Geoenergy Sci. Eng. 225, 211638. https://doi.org/10.1016/j.geoen.2023.211638.

Suo, Y., Dong, M.Y., Fu, X.J., He, W.Y., Pan, Z.J., 2024. Experimental and numerical simulation research on hot dry rock wellbore stability under different cooling methods. Geothermics 119, 102977. https://doi.org/10.1016/j.geothermics.2024.102977.

Suo, Y., Guan, W.Y., Dong, M.Y., Zhang, R.D., Wang, K., He, W.Y., Fu, X.F., Pan, Z.J., Guo, B.Y., 2025. Study on the heat extraction patterns of fractured hot dry rock reservoirs. Appl. Therm. Eng. 262, 125286. https://doi.org/10.1016/j.applthermaleng.2024.125286.

Testamanti, M.N., Rezaee, R., 2019. Considerations for the acquisition and inversion of NMR T_2 data in shales. J. Petrol. Sci. Eng. 174, 177–188. https://doi.org/10.1016/j.petrol.2018.10.109.

Tian, S.S., Bowen, L., Zeng, F., Xue, H.T., Erasova, V., Greenwell, H.C., Dong, Z.T., Zhao, R.X., Liu, J.Z., 2021. A method for automatic shale porosity quantification using an Edge-threshold automatic processing (ETAP) technique. Fuel 304, 121319. https://doi.org/10.1016/j.fuel.2021.121319.

Tian, S.S., Guo, Y.L., Dong, Z.T., Li, Z.L., 2022. Pore microstructure and multifractal characterization of lacustrine oil-prone shale using high-resolution SEM: A case sample from natural Qingshankou shale. Fractal. Fract. 6 (11), 675. https://doi.org/10.3390/fractalfract6110675.

Wang, G.C., Ju, Y.W., 2015. Organic shale micropore and mesopore structure characterization by ultra-low pressure N_2 physisorption: Experimental procedure and interpretation model. J Nat Gas Nat. Eng. 27, 452–465. https://doi.org/10.1016/j.jngse.2015.08.003.

Wang, G.P., Jin, Z.J., Liu, G.X., Wang, R.Y., Zhao, G., Tang, X., Liu, K.Q., Zhang, Q., 2023. Pore system of the multiple lithofacies reservoirs in unconventional lacustrine shale oil formation. Int. J. Coal Geol. 27, 104270. https://doi.org/10.1016/j.coal.2023.104270.

Wang, J.J., Lu, S.F., Zhang, P.F., Li, Q.F., Yin, Y.J., Li, W.B., Zhou, N.W., Chen, G.H., Yi, Y.J., Wu, C.X., 2024. Characterization of shale oil and water micro-occurrence based on a novel method for fluid identification by NMR T_2 spectrum. Fuel 374, 132426. https://doi.org/10.1016/j.fuel.2024.132426.

Wang, J.J., Zhang, P.F., Lu, S.F., Lin, Z.Z., Li, W.B., Zhang, J.J., Gao, W.Z., Zhou, N.W., Chen, G.H., Yin, Y.J., Wu, H., 2025. Insights into microscopic oil occurrence characteristics in shales from the Paleogene Funing Formation in Subei Basin. Pet. Sci. 22 (1), 55–75. https://doi.org/10.1016/j.petsci.2024.07.025.

Wang, M., Li, M., Li, J.B., Xu, L., Zhang, J.X., 2022a. The key parameter of shale oil resource evaluation: Oil content. Pet. Sci. 19 (4), 1443–1459. https://doi.org/10.1016/j.petsci.2022.03.006.

Wang, M., Li, M., Li, J.B., Xu, L., Shao, H.M., Yu, C.Q., Li, T.T., 2022b. Comparative analysis of test methods for shale oil content. Acta Petrol. Sin. 43, 17582, 1769. https://doi.org/10.7623/syxb202212007 (in Chinese).

Wu, P., Yang, J.M., Huang, R.Q., 1995. Measurement of specific surface area and pore size distribution of rocks: Static nitrogen adsorption capacity method. SY/T 6154-1995.

Wu, P., Hou, D.J., Cao, L.Z., Zhang, R.H., Wei, X.L., Ma, X.X., Zhao, Z., Chen, J.W., 2023. Paleoenvironment and organic characterization of the Lower Cretaceous lacustrine source rocks in the Erlian Basin: The influence of hydrothermal and volcanic activity on the source rock quality. ACS Omega 8 (2), 1885–1911. https://doi.org/10.1021/acsomega.2c03487.

Xiang, X., Dan, W.N., Lu, S.F., Zhang, P.F., Li, B., Cao, L.Z., Wei, Y., Li, X.W., Fan, J., Wang, J.J., Yang, Q.F., Wei, X.L., Gao, G., 2024. Insight into fluid occurrence and pore structure of lacustrine shale from the Cretaceous Tengger Formation, A'nan Sag, Erlian Basin, China. Energy Fuel 38, 12960–12977. https://doi.org/10.1021/acs.energyfuels.4c02071.

Xu, L.L., Cai, M.F., Dai, Z.X., 2025. Fractal and NMR based characterizations of multi-scale pore structure alterations in tight sandstones due to $scCO_2$-water–rock interactions. Chem. Eng. J. 508, 160898. https://doi.org/10.1016/j.cej.2025.160898.

Xu, J.J., Liu, Z.J., Bechtel, A., Sachsenhofer, R.F., Jia, J.L., Meng, Q.T., Sun, P.C., 2019. Organic matter accumulation in the Upper Cretaceous Qingshankou and Nenjiang formations, Songliao Basin (NE China): Implications from high-resolution geochemical analysis. Mar. Petrol. Geol. 102, 187–201. https://doi.org/10.1016/j.marpetgeo.2018.12.037.

Xue, H.Q., Zhou, S.W., Wang, L., Yan, G., Guo, W., Lun, Z.M., Liu, H.M., He, J.H., Fan, M., 2017. Measurement of helium and pulse decay permeability of shale. GB/T 34533-2017.

Yao, Y.B., Liu, D.M., Che, Y., Tang, D.Z., Tang, S.H., Huang, W.H., 2010. Petrophysical characterization of coals by low-field nuclear magnetic resonance (NMR). Fuel 89, 1371–1380. https://doi.org/10.1016/j.fuel.2009.11.005.

Zargari, S., Canter, K.L., Prasad, M., 2015. Porosity evolution in oil-prone source rocks. Fuel 153, 110–117. https://doi.org/10.1016/j.fuel.2015.02.072.

Zhang, J.Y., Zhu, R.K., Wu, S.T., Jiang, X.H., Liu, C., Cai, Y., Zhang, S.R., Zhang, T.S., 2023. Microscopic oil occurrence in high-maturity lacustrine shales: Qingshankou Formation, Gulong Sag, Songliao Basin. Pet. Sci. 20 (5), 2726–2746. https://doi.org/10.1016/j.petsci.2023.08.026.

Zhang, P.F., Lu, S.F., Li, J.Q., Chen, C., Xue, H.T., Zhang, J., 2018. Petrophysical characterization of oil-bearing shales by low-field nuclear magnetic resonance (NMR). Mar. Petrol. Geol. 89, 775–785. https://doi.org/10.1016/j.marpetgeo.2017.11.015.

Zhang, P.F., Yin, Y.J., Lu, S.F., Li, J.Q., Chang, X.C., Zhang, J.J., Pang, Y.M., Chen, G., Liu, Y., Li, Z., 2022. Insights into pore structures and multifractal characteristics of shale oil reservoirs: A case Study from Dongying Sag, Bohai Bay Basin, China. Energy Fuel 36, 8224–8237. https://doi.org/10.1021/acs.energyfuels.2c01763.

Zhang, P.F., Wu, H., Lu, S.F., Wang, J.J., Li, W.B., Yin, Y.J., Zhou, N.W., Chen, G.H., Yi, Y.J., Wu, C.X., 2024a. The occurrence of pore fluid in shale-oil reservoirs using nuclear magnetic resonance: the Paleogene Funing Formation, Subei Basin, Eastern China. Mar. Petrol. Geol. 167, 106986. https://doi.org/10.1016/j.marpetgeo.2024.106986.

Zhang, P.F., Lu, S.F., Wang, J.J., Li, W.B., Yin, Y.J., Chen, G.H., Zhou, N.W., Wu, H., 2024b. Microscopic occurrence and distribution of oil and water *in situ* shale: Evidence from nuclear magnetic resonance. Pet. Sci. 21, 675–691. https://doi.org/10.1016/j.engeos.2023.100270.

Zhang, P.F., Wang, J.J., Lu, S.F., Wu, H., Liu, C., Gao, W.Z., Li, W.B., Zhou, N.W., Chen, G.H., Wu, C.X., Yi, Y.J., 2025. Geochemical characteristics and paleo-environment of Lower Cretaceous lacustrine shale in the A'nan Sag, Erlian Basin, Northern China. Mar. Petrol. Geol. 178, 107420. https://doi.org/10.1016/j.marpetgeo.2025.107420.

Zhang, Q.G., Fan, X.Y., Chen, P., Ma, T.S., Zeng, F.T., 2020. Geomechanical behaviors of shale after water absorption considering the combined effect of anisotropy and hydration. Eng. Geol. 269, 105547. https://doi.org/10.1016/j.enggeo.2020.105547.

Zhang, Y.Q., Yang, S.L., Bi, L.F., Gao, X.Y., Shen, B., Hu, J.T., Luo, Y., Zhao, Y., Chen, H., Li, J., 2025. A technical review of CO_2 flooding sweep-characteristics research advance and sweep-extend technology. Pet. Sci. 22 (1), 255–276. https://doi.org/10.1016/j.petsci.2024.09.005.

Zhao, F.Z., Jiao, X.H., Xia, X.Z., Xu, S., Sun, L., Xia, Y.X., 2024. Evolution of rock pore structure and physical properties due to acidification: Recent advances and future perspectives. Adv. Geo-Energy Res. 14 (3), 238–240. https://doi.org/10.46690/ager.2024.12.08.

Zhao, L.L., Peng, R.D., Hao, P.F., Yang, Y., Zhou, H.W., 2024. Effects of pore pressure on coring-induced damage based on simulation by mesoscale stress-flow coupling numerical model. Adv. Geo-Energy Res. 14 (3), 170–186. https://doi.org/10.46690/ager.2024.12.03.

Zhao, W.Z., Bian, C.S., Li, Y.X., Li, W., Qin, B., Pu, X.G., Jiang, J.L., Liu, S.J., Guan, M., Dong, J., Shen, Y.T., 2024. "Component flow" conditions and its effects on enhancing production of continental medium-to-high maturity shale oil. Petrol. Explor. Dev. 51 (4), 826–838. https://doi.org/10.1016/S1876-3804(24)60509-4.